

AFFDL-TR-79-3078

PROPERTY OF U.S. AIR FORCE  
AEDC TECHNICAL LIBRARY  
ARNOLD AFB, TN 37389

NUMERICAL SOLUTION OF A SUPERSONIC NOZZLE  
AFTERBODY FLOW WITH JET EXHAUST

Ameer G. Mikhail

University of Dayton Research Institute  
300 College Park  
Dayton, Ohio 45469

June 1979

Final Report

September 1976 - February 1978

Approved for public release; distribution unlimited

Air Force Flight Dynamics Laboratory  
Air Force Wright Aeronautical Laboratories  
Air Force Systems Command  
Wright-Patterson Air Force Base, Ohio 45433

## NOTICE

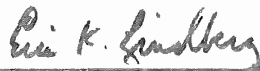
When Government drawings, specifications, or other data are used for any purpose other than in connection with a definitely related Government procurement operation, the United States Government thereby incurs no responsibility nor any obligation whatsoever; and the fact that the government may have formulated, furnished, or in any way supplied the said drawings, specifications, or other data, is not to be regarded by implication or otherwise as in any manner licensing the holder or any other person or corporation, or conveying any rights or permission to manufacture, use, or sell any patented invention that may in any way be related thereto.

This report has been reviewed by the Information Office (OI) and is releasable to the National Technical Information Service (NTIS). At NTIS, it will be available to the general public, including foreign nations.

This technical report has been reviewed and is approved for publication.



AMEER G. MIKHAIL  
Project Engineer



ERIC K. LINDBERG, Maj, USAF  
Chief, Aerodynamics and  
Airframe Branch

FOR THE COMMANDER.



PETER J. BUTKEWICZ, Col, USAF  
Chief, Aeromechanics Division

"If your address has changed, if you wish to be removed from our mailing list, or if the addressee is no longer employed by your organization please notify AFFDL/FXM, W-PAFB, OH 45433 to help us maintain a current mailing list".

Copies of this report should not be returned unless return is required by security considerations, contractual obligations, or notice on a specific document.

Unclassified

SECURITY CLASSIFICATION OF THIS PAGE (When Data Entered)

REPORT DOCUMENTATION PAGE		READ INSTRUCTIONS BEFORE COMPLETING FORM
1. REPORT NUMBER AFFDL-TR-79-3078	2. GOVT ACCESSION NO.	3. RECIPIENT'S CATALOG NUMBER
4. TITLE (and Subtitle) Numerical Solution of a Supersonic Nozzle Afterbody Flow with Jet Exhaust		5. TYPE OF REPORT & PERIOD COVERED FINAL REPORT Sept. 1976-Feb. 1978
		6. PERFORMING ORG. REPORT NUMBER UDR-TR-79-43
7. AUTHOR(s) Dr. Ameer G. Mikhail (Visiting Scientist)		8. CONTRACT OR GRANT NUMBER(s) F33615-76-C-3145
9. PERFORMING ORGANIZATION NAME AND ADDRESS University of Dayton Research Institute 300 College Park Dayton, Ohio 45469		10. PROGRAM ELEMENT, PROJECT, TASK AREA & WORK UNIT NUMBERS Project 2307N418
11. CONTROLLING OFFICE NAME AND ADDRESS Air Force Flight Dynamics Laboratory Wright-Patterson AFB, Ohio 45433		12. REPORT DATE June 1979
		13. NUMBER OF PAGES
14. MONITORING AGENCY NAME & ADDRESS (if different from Controlling Office)		15. SECURITY CLASS. (of this report) Unclassified
		15a. DECLASSIFICATION/DOWNGRADING SCHEDULE
16. DISTRIBUTION STATEMENT (of this Report) Approved for Public Release; Distribution Unlimited		
17. DISTRIBUTION STATEMENT (of the abstract entered in Block 20, if different from Report)		
18. SUPPLEMENTARY NOTES		
19. KEY WORDS (Continue on reverse side if necessary and identify by block number) Numerical Solution                      Surface Oriented Coordinates Compressible, Turbulent Flow        MacCormack's Explicit Scheme Viscous Interaction                    Exhaust Nozzles Mixing Shear Layer                    Nozzle Boattail Navier-Stokes Equations		
20. ABSTRACT (Continue on reverse side if necessary and identify by block number) Numerical solutions to the compressible turbulent Navier-Stokes equations for supersonic flow at Mach number 1.5, past an axisymmetric nozzle boattail with jet exhaust were obtained using MacCormack's explicit numerical scheme. The AGARD 10°-nozzle was considered and a total of five cases were computed showing the effects of <u>boattail geometry</u> , <u>jet-exhaust temperature</u> , <u>boattail</u> (continue on reverse side)		

Unclassified

SECURITY CLASSIFICATION OF THIS PAGE(When Data Entered)

block 20 continued

wall temperature and the differences with the corresponding two-dimensional case. It was established that the hot boattail surface reduces the pressure drag significantly as does the hot jet exhaust when compared with the cold wall, cold exhaust case. The present approach can be used directly for boattailing nozzles for minimum pressure drag, as well as for a parametric study for aircraft designers.

Unclassified

SECURITY CLASSIFICATION OF THIS PAGE(When Data Entered)

## FOREWORD

This report is the result of work carried on in the Computational Aerodynamics Group, Aeromechanics and Airframe Branch, Aerodynamics Division, Air Force Flight Dynamics Laboratory. It was performed by Dr. Ameer G. Mikhail, visiting scientist, under Project 2307N418, "Computational Fluid Dynamics". Dr. Wilbur L. Hankey is the AFFDL Task Engineer.

Dr. Mikhail performed the work from September 1976 through February 1978 and released the report in December 1978.

The author would like to express his thanks to Dr. Wilbur L. Hankey and Joseph S. Shang, of the Flight Dynamics Laboratory for their valuable suggestions and contributions to this work.

# TABLE OF CONTENTS

SECTION		PAGE
I	INTRODUCTION	
	1. General Review	1
	2. Flow Structure	2
	3. The Present Approach	4
II	FORMULATION OF THE PROBLEM	
	1. The Specific Test Case Chosen	7
	2. Coordinate System	8
	3. The Governing Equations	15
	4. Turbulence Models	20
	5. Boundary Conditions	23
III	THE NUMERICAL PROCEDURE	
	1. Splitting Procedure	26
	2. Stability Condition, Estimated Maximum Time Step	27
	3. Numerical Damping	29
	4. Implementation of the Boundary Conditions	31
	5. Initial Conditions	32
IV	RESULTS AND DISCUSSION	
	1. Data of Experiments and the Cases Computed	33
	2. Computation Details	34
	3. Comparison with the Experiment	35
	4. Boattail Geometry Effects	37
	5. Hot Exhaust Effects	39
	6. Boattail Surface Temperature Effects	40
	7. The Two-Dimensional Case	41
V	SUMMARY AND RECOMMENDATIONS	
	1. Summary	43
	2. Recommendations for Further Studies	44
	FIGURES	45
	REFERENCES	58

# LIST OF ILLUSTRATIONS

FIGURE		PAGE
1a	Weakly Underexpanded Nozzle.	3
1b	Highly Underexpanded Nozzle.	4
2	Geometry of the AGARD 10°-Nozzle.	8
3	The AEDC Nozzle Boattail Geometry.	9
4	Nozzle Pressure Ratio Definition.	10
5	Mesh Points Distribution.	12
6a	Mesh Points Near the Nozzle Lip.	14
6b	Mesh Points Near the Nozzle Lip.	15
7	Placement of Nozzle Exit Conditions.	16
8	The Affine Distribution.	17
9	Boundary Conditions Placement for the Jet Flow.	25
10	Nomenclature for Estimating the Maximum Time Step.	28
11a	Development of the Surface Pressure Coefficient.	36
11b	Axial Variation in $u$ and $P$ .	38
12	Domain of Present Interest.	45
13	Eddy Viscosity Models.	46
14	Boundary Conditions in the Physical and Computational Domain.	47
15	Comparison with Experiment.	48
16	Influence of Boattail Geometry on Pressure Coefficient Distribution.	49
17	$C_p$ For Different Cases.	50
18	Axial Variation in $u$ , $p$ & $T$ .	51
19	Density Contours.	52
20	Mach-Line Contours.	53

# LIST OF ILLUSTRATION (Concluded)

FIGURE		PAGE
21	Static Temperature Contours.	54
22	Static Temperature Profiles in the Mixing Region.	55
23	Axial-Velocity Profiles in the Mixing Region.	56
24	The Flow Field and Stream Function.	57



## LIST OF SYMBOLS

AEDC	Arnold Engineering Development Center, Tallahoma, Tennessee
$c_p$	Pressure Coefficient, $(P - P_{\infty e}) / (1/2 \rho_{\infty} U_{\infty}^2)$
$C_p, C_v$	Specific heats of the gas
$e$	Specific total internal energy
$i, j$	Indices indicating location of the node point in the computational domain
$j_o$	Exponent parameter that equals 1 or 0 for axisymmetric or two-dimensional flow, respectively
$J_c$	Jacobian of the coordinate transformation
$M$	Mach number $\sqrt{u^2 + v^2} / \sqrt{(\gamma RT)}$
NPR	Nozzle pressure ratio, defined as $(P_{oj} / P_{\infty e})$
$P, P_o$	Static and total pressure, respectively
$Pr$	Prandtl number, laminar flow
$Pr_t$	Prandtl number, turbulent flow
$R$	The gas constant
$r, x$	Cylindrical coordinates in the radial and axial directions, respectively
$T, T_o$	Static and total temperature, respectively
$u, v$	Velocity components along the $x$ and $r$ directions, respectively

### Greek Symbols

$\alpha$	Characteristic angle of supersonic flow
$\alpha_o$	Coefficient in MacCormack's damping formulation
$\beta$	Normal stress damping factor
$\gamma$	Ratio of specific heats (taken as 1.4)

## LIST OF SYMBOLS (Concluded)

$\varepsilon$	Coefficient of turbulent viscosity
$\eta, \xi$	Transformed coordinates for the physical (r,x) variables
$\lambda_t$	Turbulent second coefficient of viscosity
$\mu$	Coefficient of molecular viscosity
$\rho$	Fluid density

### Subscripts

a	Denotes "ambient" condition
e	Denotes the external flow over the boattail surface
j	Denotes the jet flow
w	Denotes wall surface condition
$\infty$	Denotes free stream condition for the external flow

SECTION I  
INTRODUCTION

1. GENERAL REVIEW

As a step toward the realization of the concept of a "Numerical Wind Tunnel", the unified use of the full continuum flow equations (Navier-Stokes) was employed to yield numerical solutions for supersonic flow past nozzle-afterbody configurations for arbitrary nozzle geometries and flow conditions. This particular flow problem is usually investigated through wind tunnel testing. The complexity of the flow structure and the lack of confidence in existing numerical capabilities are among the factors that deterred investigators from attacking the problem using the present approach. Numerical approaches, however, were tried by several investigators<sup>1-3</sup> using patching procedures for different regions, or other restrictive assumptions such as solid plume simulators.

This work was done for the purpose of developing different techniques for estimating the aerodynamic properties of aircraft components as a step forward toward the design integration goal. This work is the second stage of a two-stage project. The completed work of the air intake inlet problem<sup>4</sup> was the first stage.

The aerodynamics of propulsion elements in aircraft and rockets plays a significant role in determining the importance of the airborne vehicle. The pressure drag of the jet engine exhaust nozzle, for example, contributes considerably to the total drag of the air worthy jet propelled vehicle. Its minimization, therefore, receives considerable attention by experimentalists for optimum boattailing. The pressure drag on the nozzle surface can not be properly computed without considering the mutual effects of the exhaust jet and the outer stream. Therefore, the domain of mutual influence between the outer and the existing jet flow must be considered. This mutual effect is being considered by the present approach.

This particular flow problem is directly related to the mixing of two supersonic axisymmetric streams. It also involves most of the flow features that can be observed in a compressible supersonic flow field. Turbulent boundary layer, separation, free reattachment (not on a surface), lip shock, separation shock, barrel shock, shock intersection and reflection, Mach disk, slip surface, free turbulent mixing, "inviscid" plume structure and other interesting details can be observed.

The basic flow structure is described briefly next.

## 2. FLOW STRUCTURE

Depending on the nozzle pressure ratio (NPR) which will be defined here as  $NPR = P_{oj}/P_{\infty e}$  for reasons discussed in Section II, the flow structure can assume one of two familiar modes.

Considering only underexpanded nozzles, and if the NPR is low (lower than a certain critical value  $NPR_{cr}$ ) the turning angle of the exiting flow at the nozzle wall will be relatively small, allowing the expansion fan to reflect at the center line  $r = 0$ , with incident and reflected angles almost equal to  $90^\circ$ . This will result in the familiar repeated "diamond" pattern, as shown in Figure 1.

If the nozzle boattail outline curve is of steep gradient, flow separation may occur on the surface, however, reattachment is not expected to occur at the solid wall, but rather down stream. The separation shock may coalesce with the weak attachment shock forming one  $\lambda$  (lambda) structure. Two circulating flow bubbles, or more, are mostly expected depending on the geometry of the nozzle lip and the NPR. The mixing between the external and the jet streams will take place along the "inviscid plume boundary" which disappears, giving way to a widening mixing "layer" that increases in "width" and finally intersects with the line of symmetry.

For larger NPR (larger than the critical NPR) the jet flow turning angle at the nozzle lip is relatively large, allowing the expansion fan to reflect at the center line with angle

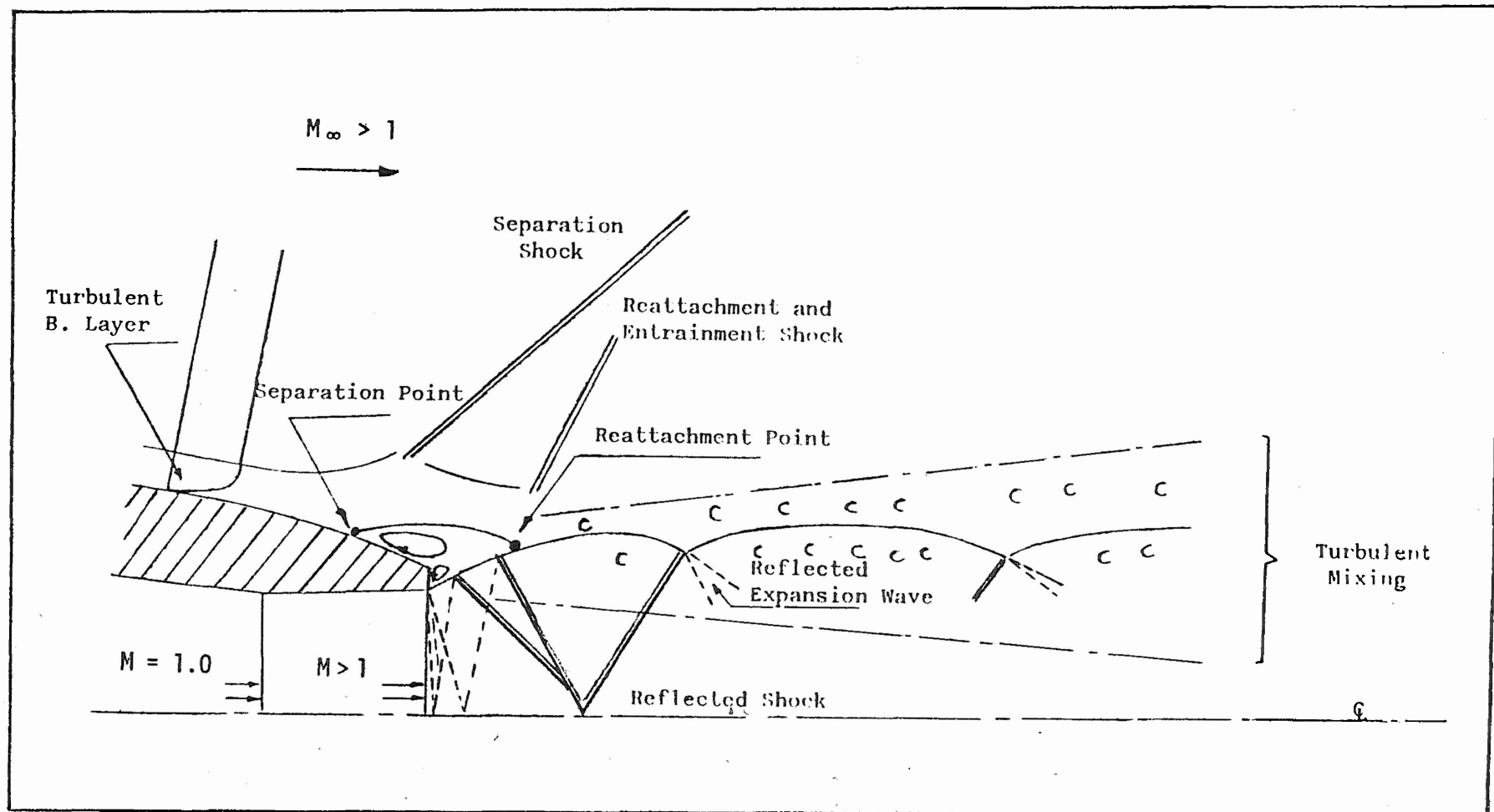


Figure 1a. Weakly Underexpanded Nozzle.

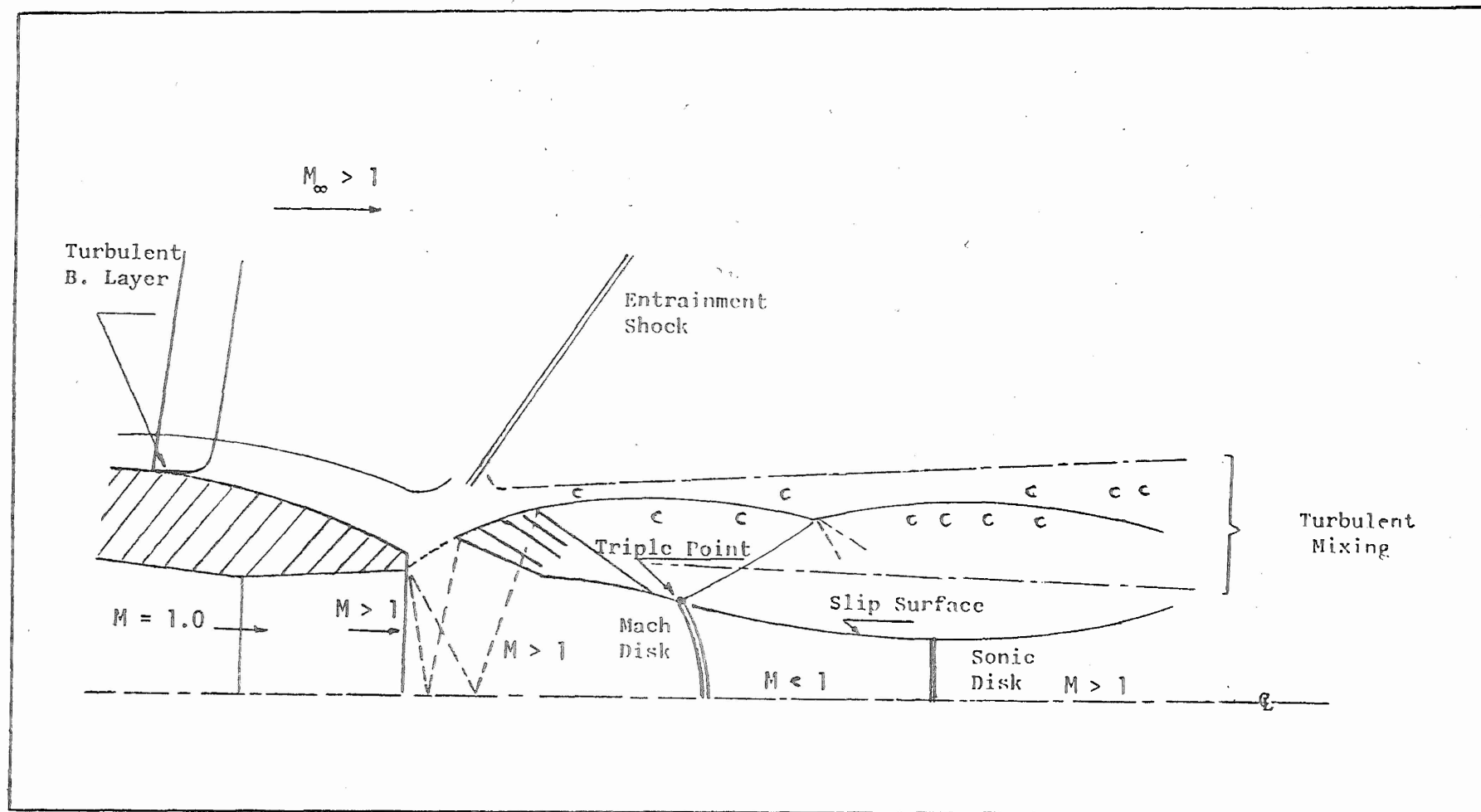


Figure 1b. Highly Underexpanded Nozzle.

smaller than  $90^\circ$ , which reflects again at the fictitious "inviscid plume boundary" in a form that allows them to coalesce forming one shock known as the barrel shock before they intersect with the center line, as shown in Figure (1.1B) with the familiar triple point formation. The intersection at the center line is in the form of a curved Mach disk with subsonic region behind it. A slip surface initiates at the triple point and extends behind the Mach disk.

For the same boattail geometry, flow separation on the boat-tail surface is expected to start earlier upstream for the high NPR. In addition, the large flow turning angle will then cause the shock formed to be stronger. The viscous interaction is much stronger in this case and no well-defined reattachment point is expected.

### 3. THE PRESENT APPROACH

The domain of present interest is shown in Figure (1), where the viscous interaction between the external and jet streams is a dominant factor. Therefore, the use of the complete Navier-Stokes equations is necessary to capture such interactions. The equations will be solved uniformly all over the domain of interest, thus avoiding the need for any patching procedure as those of References (3) and (5). This uniformity also enables the true presentation and computation of the mutual effects of the jet and the boattail surface flow conditions and vice versa, without the need for superposition of effects in an iterative procedure to correct for the mutual influences.

A coordinate transformation will be used to map the present domain onto a square of unit length. The mesh points in that transformed plane are uniformly spaced, while the corresponding points in the physical domain are highly nonuniform for the proper concentration required for turbulent flow.

Since the present case of interest is only for the supersonic flow at  $M_\infty = 1.5$ , the numerical scheme chosen should be a shock capturing method since the details and exact location of the

shocks is not known a priori. Therefore, MacCormack's time dependent, explicit scheme will be favored for its proven reliability. Although this explicit scheme, as most explicit schemes, have severe stability restrictions, it is to be understood here, that it is not the task of the present work to test and utilize more efficient schemes, which are relatively recent leaving that to simpler problems for future investigation.

The present work is considered pioneering due to the very little known information about the flow conditions in the immediate vicinity of the computational region. In addition, several engineering judgements had to be made regarding the flow conditions, shape and extension of the region of computation, the coordinate system chosen, mesh point distribution and the turbulence model used.

Therefore, the major objective in this work is to show that such a complex flow can be computed successfully, rather than emphasizing accuracy or computational efficiency.



## SECTION II

### FORMULATION OF THE PROBLEM

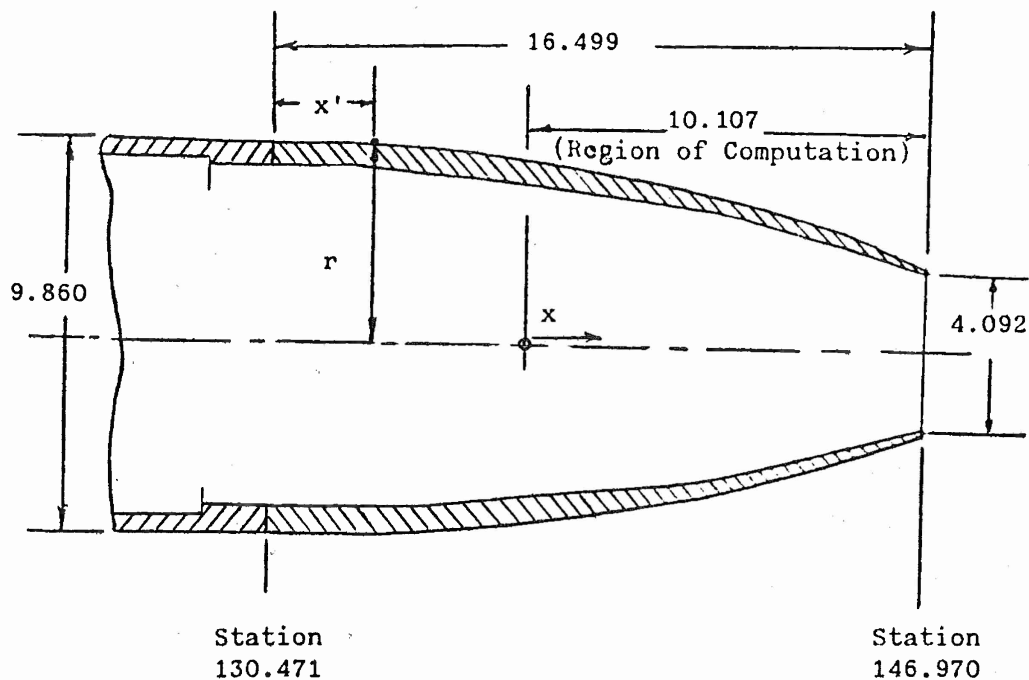
In this section, details of the steps of formulation are presented. The choice of the test case, the coordinate mapping used, the form of the governing equations, boundary conditions specified, turbulence model and other pertinent details are discussed.

#### 1. THE SPECIFIC TEST CASE CHOSEN

To test and verify the numerical computation, experimental results must be available for comparison. Limited experimental results are available for the almost parallel mixing of supersonic streams. For nonparallel streams, there are many results. For example, results for single jet exhausting into static air, or the mixing of exhaust with subsonic external stream.

In Reference (6), three AGARD convergent nozzles were tested, but only the boattail surface pressure was reported. The three nozzles are denoted by 10°, 15°, 25° nozzles and were chosen by the AGARD Organization to study the deviation in the measurements reported by the different testing facilities for the same geometries. In the mentioned reference, measurements for cases with hot jet exhaust and different free stream Mach number (supersonic and subsonic) were also presented for some of these three geometries. No other flow variables or information down the nozzle exit or on the boattail surface were provided.

For the present work, the 10°-nozzle was chosen with Mach number  $M_{\infty e} = 1.5$ , at NPR = 7.09. The exact geometry of that nozzle is given in Figure (2.1). The experiments on that nozzle were run in the AEDC supersonic wind tunnel, with Reynolds number =  $2.5 \times 10^6$  per foot. At the station 130.47" from the tip nose of the engine model, the local Reynolds number is then  $27.18 \times 10^6$  signifying fully turbulent flow conditions.



DIMENSIONS IN INCHES

$x'$	$r$	$x'$	$r$	$x'$	$r$	$x'$	$r$
0	4.930	4.420	4.760	8.857	4.191	13.294	3.252
0.230	4.926	4.667	4.736	9.104	4.154	13.541	3.173
0.476	4.923	4.913	4.711	9.350	4.115	13.787	3.089
0.723	4.918	5.160	4.684	9.597	4.075	14.034	3.002
0.969	4.915	5.406	4.654	9.843	4.036	14.280	2.914
1.216	4.913	5.653	4.624	10.090	3.993	14.527	2.820
1.462	4.908	5.899	4.595	10.336	3.949	14.773	2.726
1.709	4.903	6.146	4.565	10.583	3.905	15.020	2.626
1.955	4.895	6.392	4.536	10.879	3.858	15.266	2.524
2.202	4.889	6.639	4.504	11.076	3.809	15.513	2.419
2.448	4.881	6.885	4.472	11.322	3.760	15.636	2.366
2.695	4.874	7.132	4.440	11.569	3.707	15.759	2.315
2.941	4.864	7.378	4.407	11.815	3.653	16.006	2.214
3.188	4.854	7.625	4.376	12.062	3.592	16.252	2.125
3.434	4.841	7.871	4.341	12.308	3.530	16.499	2.046
3.681	4.824	8.118	4.304	12.555	3.464		
3.927	4.807	8.364	4.267	12.801	3.397		
4.174	4.785	8.611	4.228	13.048	3.326		

Figure 2. Geometry of the AGARD 10°-Nozzle.



Another nozzle geometry was used by the AEDC at the early stage of its study, however no experimental data is available for supersonic external flow. This nozzle will be denoted here as the AEDC early model. This geometry was used in the present work to illustrate the effect of the boattail geometry on the surface  $c_p$  distribution in comparison with the result for the AGARD 10° nozzle. Details of this nozzle geometry are given by Figure (2.2).

It is to be noted that the value 7.09 for the NPR as defined here by  $P_j/P_{\infty e}$  is not "very" high. Usually the NPR is defined in the case of a right cylinder with no external flow, so as to reflect the ratio between the static pressure value at the exit plane,  $P_j$ , and the ambient value in the immediate vicinity of the nozzle lip,  $P_a$ , as demonstrated in Figure (2.3 a,b). However, for curved boattail walls with external flow, the value of the static pressure at the lip,  $P_a$ , as of Figure (2.3a) is not known a priori. Besides,  $P_a$  at the nozzle lip is greatly different and smaller (for supersonic flow) than the value of the undisturbed pressure of the external flow,  $P_e$ . Therefore, in this case, since the NPR cannot be defined as  $P_j/P_a$ , it is usually defined as  $P_j/P_{\infty e}$ . For  $M_{\infty e} = 1.5$ , the ratio  $P_j/P_{\infty e}$  is only 3.7 for the corresponding ratio  $P_j/P_{0e}$  of value 7.09. Finally, it is to be noted that the critical value  $NPR_{cr} = 2. - 2.4$ , is only valid for the case (b) of Figure (2.3), where here NPR denotes  $P_j/P_a$ .

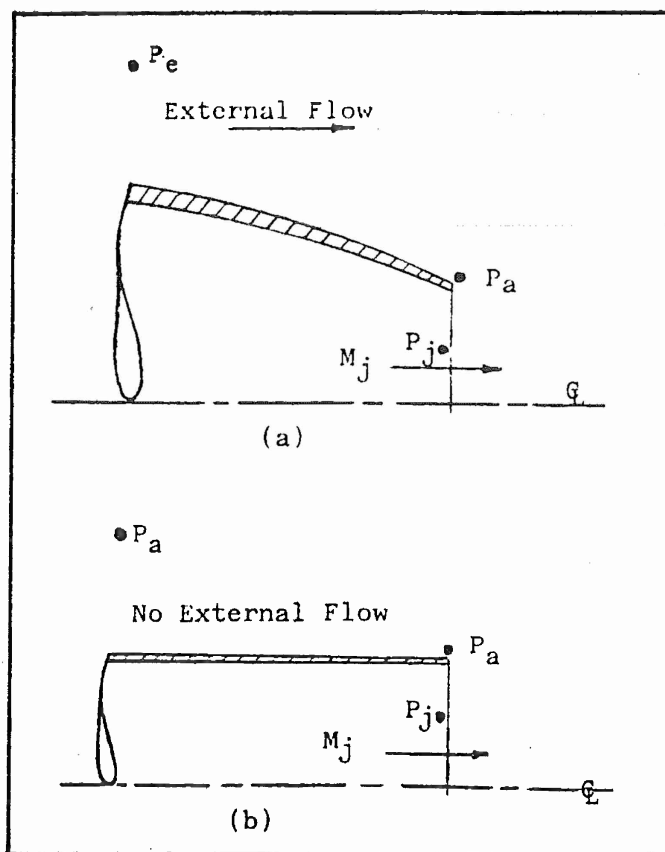


Figure 4. Nozzle Pressure Ratio Definition.

## 2. COORDINATE SYSTEM

### Domain of Computation

The cylindrical coordinates  $(r, \theta, x)$  were used for this axisymmetric geometry where  $r$  is in the radial direction and  $x$  is along the axis of symmetry. The  $\theta$  dependency is dropped for the axisymmetry formulation. Of the 16.0 inches of the nozzle body shown in Figure (2.1), only 10.0 inches were considered to minimize the number of points needed for computation. A height of 12.0 inches was taken normal to the boattail surface representing about four times the estimated boundary layer thickness at that location. Along the axis, 16.0 inches representing about four times the exit diameter was considered appropriate, ensuring that the "far field" boundary conditions will be in the supersonic region if a Mach disc followed by the subsonic region should occur at higher NPR.

### Coordinates Transformation

The  $(r, x)$  physical domain of Figure (2.4) was mapped to a unit square in the computational plane  $(\eta, \xi)$  through the mapping procedure described in Reference (7). The  $\eta = \text{constant}$  lines are aligned parallel to the boattail wall surface and the  $\xi = \text{constant}$  lines are in the direction normal to the boattail surface. Along the  $\eta = \text{constant}$  lines, 39 points were used, and 30 points were utilized along the  $\xi = \text{constant}$  lines.

It was found difficult, as will be discussed next, to obtain the proper source distribution necessary for the procedure of Reference (7) that would cause the coordinate lines to satisfy all the requirements. Therefore, an averaging procedure was used, with a sacrifice in the total smoothness of the transformation coefficients  $\eta_r, \eta_x, \xi_r$  and  $\xi_x$  (subscripts denote differentiation with respect to the subscript variable).

In the mentioned mapping procedure, the point distribution should be provided along the boundary afhjk of Figure (2.4). The appropriate points along af as well as the corresponding points along hj were chosen. Along the boundaries fh and aj, the

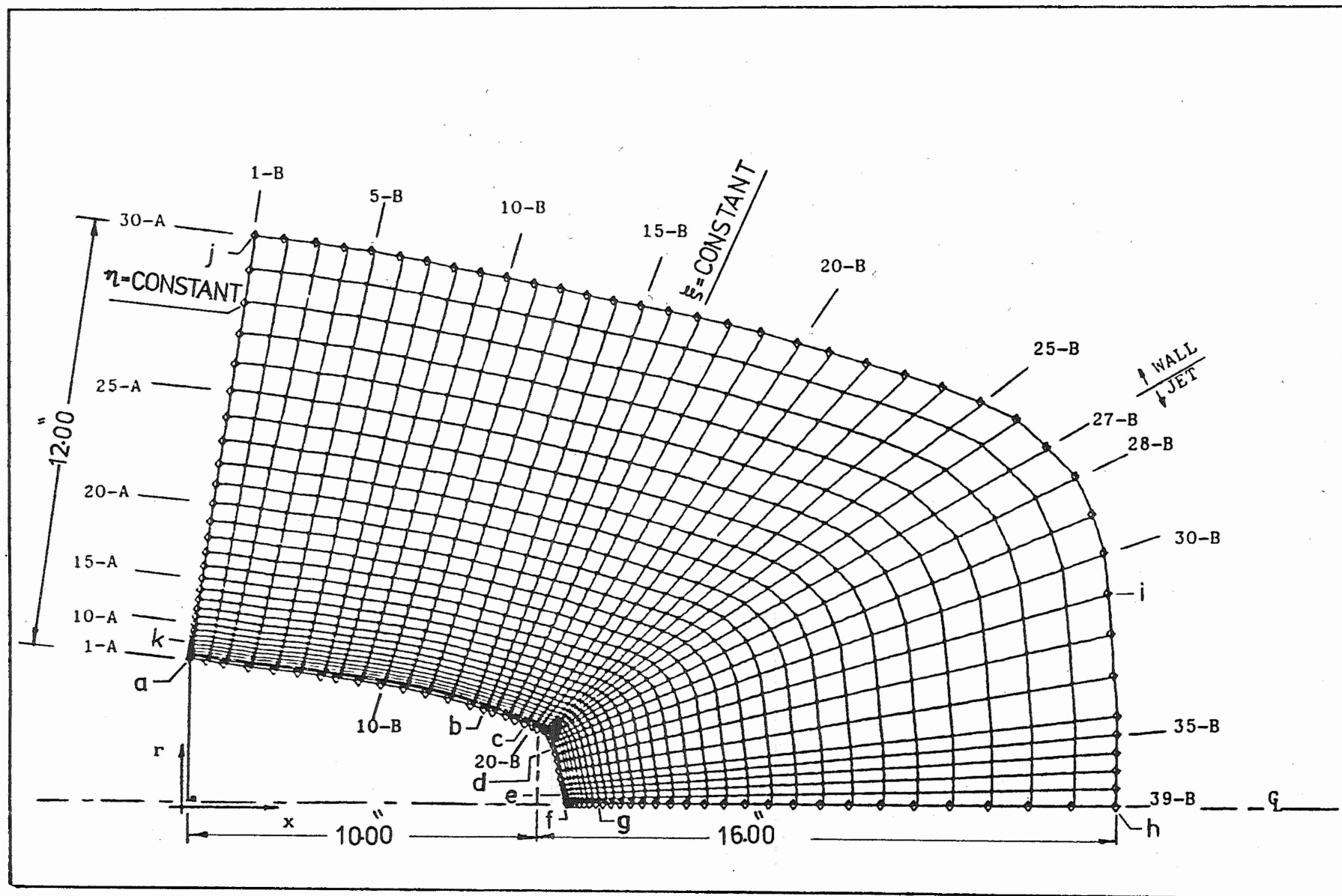


Figure 5. Mesh Points Distribution.

distributions were basically similar, both with exponential growth allowing the first point to be about 0.07 inches from the wall and the last point 12.0 inches away. Although 0.07 inches is considered very large with regard to turbulent flow, it was used here to allow relatively large time step for the time dependent method as will be discussed later in this section. This fact will therefore lead to large inaccuracies in the estimated values for the viscous drag coefficient  $c_f$ . However  $c_p$ , which is the main parameter of interest here, is not greatly sensitive to the mesh step size as long as it is small enough.

#### Requirements in the Chosen Coordinates

The following requirements were set for determining the appropriate coordinate system. They also represent a difficulty in determining the proper source distribution for the method of Reference (7).

1. Maintaining orthogonality to the boattail surface, especially near the surface, to simplify the application of the derivative boundary conditions. This had to be relaxed in the region of Figure (2.4) to allow smooth distribution of the corresponding points on the boundary  $ij$ .

2. Orthogonality is also desirable near the outer boundary  $hj$  for simple application of the "no change" boundary condition. This requirement was relaxed locally.

3. More dense points are needed in the region  $bc$ , compared to  $ab$ , so that flow separation can be detected and numerical instability is possibly avoided.

4. In region  $cf$ , a small step size is needed near the nozzle lip in the region  $cd$ , however, larger steps can be allowed in region  $de$ . Relatively small steps in the region  $ef$  are needed near the center line to minimize the error of the described derivative boundary conditions especially when only first order accurate differences are used at the boundaries.

5. More points are needed near the wall, in the region  $ak$  to capture the large gradient of the turbulent boundary layer. However, if the coordinate lines  $\eta = \text{constant}$  are parallel to the wall  $af$ , it will be very difficult to get this distribution to be different in the region  $fg$  where not as many points might be required. In fact, even for jet flow exiting at  $M_j = 1.001$ , with lines of characteristics almost normal to the center line  $fh$ , no difficulty was encountered with relatively wide spread points.

6. The coordinate lines in the region between  $df$  and  $ih$  should be as orthogonal as possible to the center line  $fh$ , to simplify the implementation of the boundary conditions.

#### Remarks and Comments on the Present Coordinates

The sharp corner "A" of nozzle lip was first avoided by placing the points ( $I = 24$ , 25) on each side as shown in Figure (2.5A). This was done to have continuous transformation derivatives. However, it was found essential, later, to have the jet exit plane and the lip line be substituted by a curve  $AB$  as that of Figure (2.5B). This curve was chosen arbitrarily and represents an additional parameter for the numerical procedure.

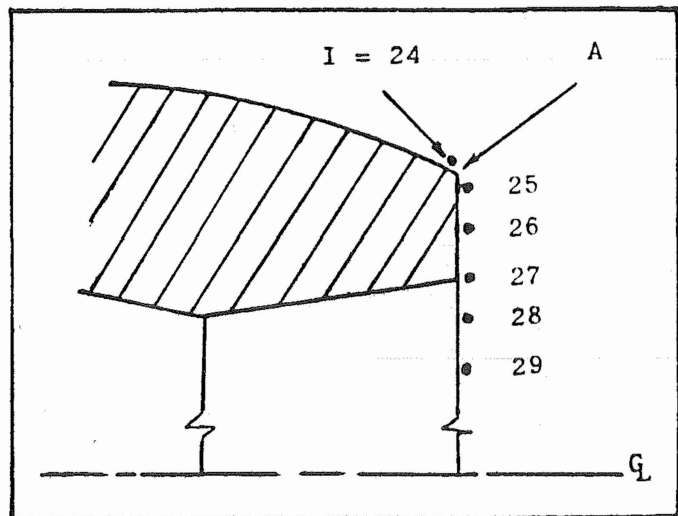


Figure 6a. Mesh Points Near the Nozzle Lip.

Although placing the boundary conditions on that curve instead of the original straight line, will not represent a large approximation as will be seen in Section (2.5), it is undoubtedly an undesirable parameter. The possible interpretation will also



be discussed in Section (2.5). The exact geometry of the back shoulder is presented in Figure (2.6).

As was mentioned earlier, two different nozzle geometries were examined. The AEDC early model was first utilized and the grid point distribution along the wall is shown in Figure (2.6).

When the AGARD 10°-nozzle was used, a different and more uniform point distribution, as shown by curve A

in Figure (2.7) was attempted. However, this new distribution together with the resulting transformation coefficients led to blow ups during computations due to negative physical quantities near the nozzle lip. Surprisingly, this problem was alleviated when the point distribution for the new geometry was chosen to be affine to the distribution for the AEDC model. By affine it is meant that only the  $r$ -coordinate changes, keeping the  $x$ -location of the points the same. Both the affine and the more uniform (but not affine) distributions are shown in Figure (2.7). The possible interpretation for this undesirable behavior is that the affine distribution have more points near the nozzle lip, where large gradients in pressure and density occur.

### 3. THE GOVERNING EQUATIONS

The Navier-Stokes equations for axisymmetric and two-dimensional turbulent flows can be written in the following familiar form, where the dependent variables  $u$ ,  $v$ ,  $e$  are mass-averaged as described in Reference (8), while  $\rho$  and  $P$  are the mean (time averaged) state variables.

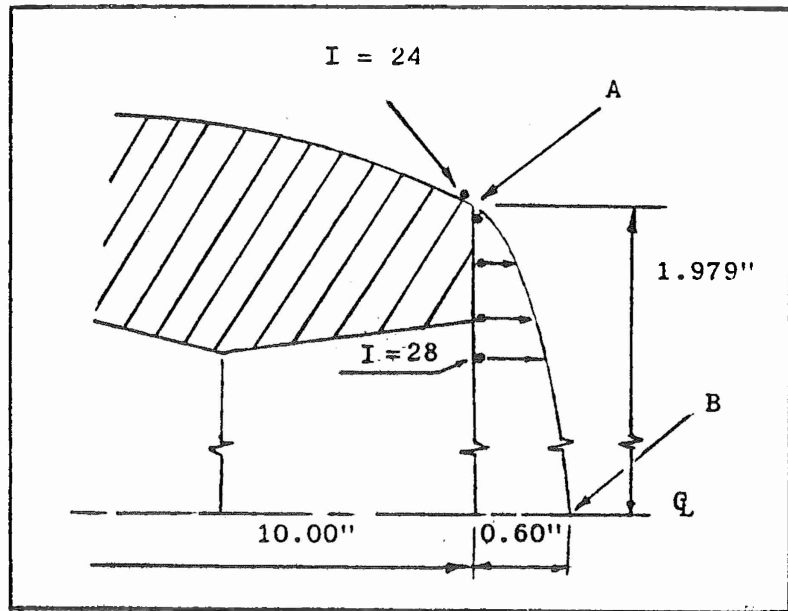


Figure 6b. Mesh Points Near the Nozzle Lip.

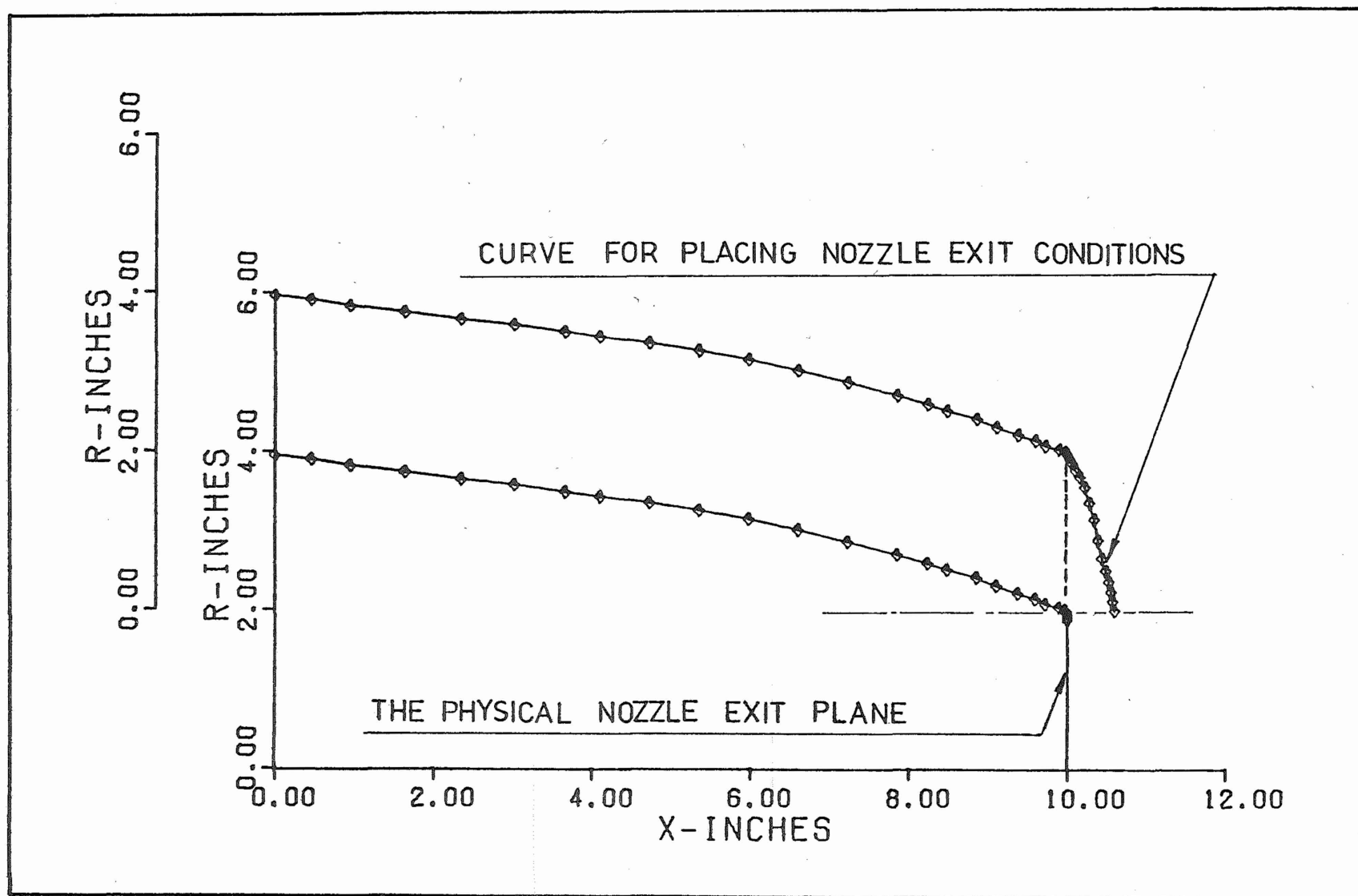


Figure 7. Placement of Nozzle Exit Conditions.

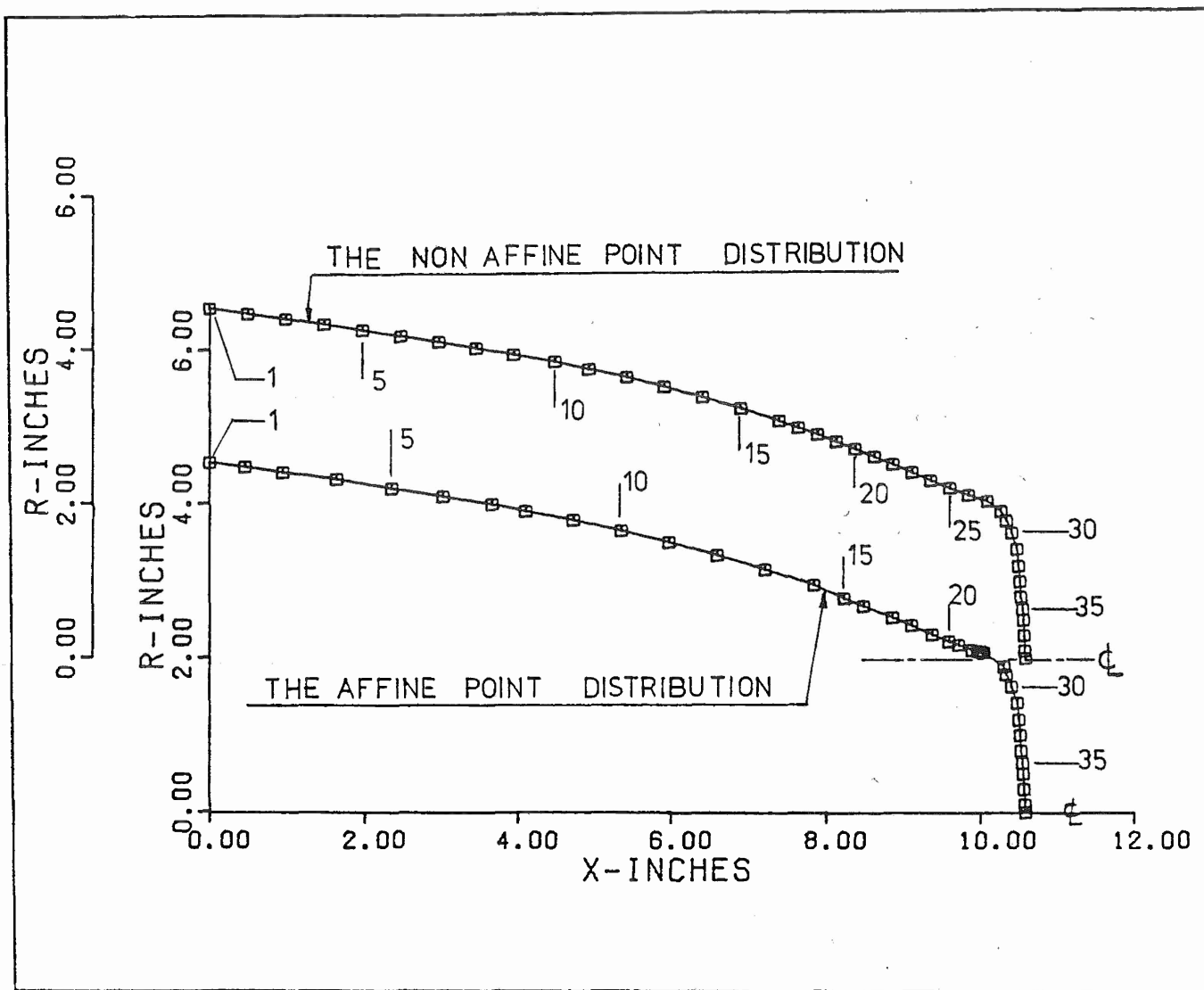


Figure 8. The Affine Distribution.

$$\frac{\partial U}{\partial t} + \frac{\partial F}{\partial x} + \frac{1}{r j_0} \frac{\partial (r^{j_0} G)}{\partial r} = j_0 \cdot \frac{H}{r j_0} \quad (2.1)$$

where  $j_0 = 1$  or  $0$  for axisymmetric and two-dimensional flow cases respectively, and

$$U = \begin{pmatrix} \rho \\ \rho u \\ \rho v \\ \rho e \end{pmatrix}, \quad F = \begin{pmatrix} \rho u \\ \rho u u - \sigma_{xx} \\ \rho u v - \tau_{xr} \\ \rho u e + \dot{q}_x - \sigma_{xx} u - \tau_{xr} v \end{pmatrix} \quad (2.2)$$

$$G = \begin{pmatrix} \rho v \\ \rho u v - \tau_{xr} \\ \rho v v - \sigma_{rr} \\ \rho v e + \dot{q}_r - \tau_{xr} u - \sigma_{rr} v \end{pmatrix}, \quad H = \begin{pmatrix} 0 \\ 0 \\ -\sigma_+ \\ 0 \end{pmatrix}$$

where

$$\left. \begin{aligned} \sigma_{xx} &= -P + \lambda_t (\nabla \cdot \vec{U}) + 2(\mu + \epsilon) \frac{\partial u}{\partial x}, \\ \sigma_{rr} &= -P + \lambda_t (\nabla \cdot \vec{U}) + 2(\mu + \epsilon) \frac{\partial v}{\partial r}, \\ \tau_{rx} &= \tau_{xr} = (\mu + \epsilon) \left( \frac{\partial u}{\partial r} + \frac{\partial v}{\partial x} \right), \\ \sigma_+ &= -P + \lambda_t (\nabla \cdot \vec{U}) + 2(\mu + \epsilon) \frac{v}{r}, \\ e &= C_v T + \frac{1}{2} (u^2 + v^2), \\ \dot{q}_x &= -C_p \left( \frac{\mu}{P_r} + \frac{\epsilon}{P_{rt}} \right) \frac{\partial T}{\partial x}, \\ \dot{q}_r &= -C_p \left( \frac{\mu}{P_r} + \frac{\epsilon}{P_{rt}} \right) \frac{\partial T}{\partial r} \end{aligned} \right\} \quad (2.3)$$

and where

$$\nabla \cdot \vec{U} = \frac{\partial u}{\partial x} + \frac{\partial v}{\partial r} + j_o \frac{v}{r} \quad (2.4)$$

The perfect gas relation was used for air, i.e.

$$P = \rho RT \quad (2.5)$$

and the coefficient of viscosity was assumed to vary with temperature according to Sutherland's law

$$\mu = (2.27 \times 10^{-8}) \frac{T^{1.5}}{(T + 198.6)} \quad (\text{lb} \cdot \text{sec} / \text{ft}^2) \quad (2.6)$$

The laminar and turbulent Prandtl numbers are assumed constant and of values  $P_r = 0.72$  and  $P_{rt} = 0.9$  respectively.

The second coefficient of viscosity was chosen as

$$\lambda_t = \frac{-2}{3} (\mu + \epsilon) \cdot \beta \quad (2.7)$$

where  $\beta$  is a constant less or equal to +1.0 (usually it is negative and of order -10). It can, of course, vary as a function of  $(r, x)$ . It is used during the early stage of computation to help damping large transient pressure gradients as described and used in Reference (9). However, after the numerical solution stabilizes itself,  $\beta$  should be set back to +1.0 to represent the true Navier-Stokes equations.  $\beta$  is referred to as the normal stress damping coefficient because although it influences particle friction, it only occurs in the normal stress components. In addition, it is only effective when  $\nabla \cdot \vec{U}$  is relatively large, which is the case across shocks and large pressure gradients in general.

For numerical computation, Equation (2.1) is written in the transformed plane of  $(\eta-\xi)$  as

$$\begin{aligned} \frac{\partial U}{\partial t} + \left[ \xi_x \frac{\partial F}{\partial \xi} + \frac{1}{r j_o} \xi_r \frac{\partial (r j_o G)}{\partial \xi} \right] \\ + \left[ \eta_x \frac{\partial F}{\partial \eta} + \frac{1}{r j_o} \eta_r \frac{\partial (r j_o G)}{\partial \eta} \right] = j_o \cdot \frac{H}{r j_o} \end{aligned} \quad (2.8)$$

where now  $\eta$  and  $\xi$  are the independent variables and  $\xi_x$ ,  $\xi_r$ ,  $\eta_x$ , and  $\eta_r$  are the four transformation derivatives obtained numerically from the mapping procedure. In addition, it is expected that solving these equations numerically is more difficult than that of Equation (2.1), due to the stiffness introduced by the stiff transformation derivatives for the present geometry.

Equations (2.8) are in weak conservative form due to the source term arising only for the axisymmetry formulation, and due to the varying coefficients in front of the derivatives. These equations can be reduced to a better conservation form for the axisymmetry case and to the strong conservation form for the corresponding 2-D case, if the dependent variables are regrouped according to Viviand<sup>10</sup>, the form of the equation would then be

$$\begin{aligned} \frac{\partial}{\partial t} \left[ \frac{r^j_{oU}}{J_c} \right] + \frac{\partial}{\partial \xi} \left[ \frac{\xi_x}{J_c} \cdot r^j_{oF} + \frac{\xi_r}{J_c} \cdot r^j_{oG} \right] \\ + \frac{\partial}{\partial \eta} \left[ \frac{\eta_x}{J_c} \cdot r^j_{oF} + \frac{\eta_r}{J_c} \cdot r^j_{oG} \right] = \left[ j_o \frac{H}{J_c} \right] \end{aligned} \quad (2.9)$$

where  $J_c$  is the Jacobian of the transformation defined as  $J_c = \xi_x \eta_r - \xi_r \eta_x$ .

Although this form was not used in the present work it is recommended for future formulations for better shock capturing ability and possibly better accuracy.

#### 4. TURBULENCE MODELS

The experimental tests for the nozzle geometry under consideration (the AGARD 10°-nozzle) were run at Reynolds number of  $2.5 \times 10^6/\text{ft}$ . Therefore, the flow is expected to be fully turbulent with a Reynolds number in excess of  $25.0 \times 10^6$  at the end of the long cylindrical forebody at station 130.47 inches downstream of the nose tip. This station marks the beginning of the nozzle boattail, 6.49 inches upstream of the station where computations begin (see Figure (2.2)).

Complicated eddy viscosity models can be found in the literature for many flow patterns including the axisymmetric wake problem. It has not yet been demonstrated that the use of sophisticated or high order closure models would necessarily yield better results in general. Many models for the free shear layers, jets and wakes using the turbulent kinetic energy and other concepts can be found for example in References (11) and (12).

It was decided here to use the simplest model in the complex mixing region. The eddy viscosity model in the computational domain was split into different models in different regions as shall be explained.

The computation domain is split into three regions as shown in insert A of Figure (3). In region I, the simple two-layer algebraic model of Reference (13) for flat plate is used here since the effect of axisymmetry was estimated to be minor at this flow condition for a cylinder with a diameter of approximately 4.0 inches. The inner region for that model is formulated as

$$\epsilon_i = \rho \left[ 0.4 r_n \left( 1 - e^{-\frac{r_n \sqrt{\tau_w \rho}}{26\mu}} \right) \right]^2 \cdot \left| \frac{\partial U_t}{\partial r_n} \right|$$

and the outer region model is formulated as:

$$\epsilon_o = 0.0168 \rho U_e \delta_{inc}^*$$

where:

- $r_n$  is the normal distance measured from the boattail wall
- $\tau_w$  is the wall shear stress
- $U_t$  is the tangential velocity in direction parallel to the wall
- $U_e$  is the average tangential velocity outside the boundary layer of the velocity profile at that station, here taken as  $U_t$  at the point of index  $j = 15$  (approximately  $r_n \approx 2.0$ ")

$$\delta_{inc}^* = \int_0^\delta \left( 1 - \frac{U_t}{U_e} \right) dr_n$$

In region III, the eddy viscosity for a jet is used which increases in the axial direction while remaining constant in planes normal to the axis. The following model was used:

$$\epsilon_{III} = \epsilon_{in} (1 + S)$$

where

- S is the dimensionless distance along the "rays" of the coordinates  $\xi = \text{constant}$ , measured from the jet exiting station. ( $S=0$  at the exit plane and  $S=1$  at the far-field boundary)
- $\epsilon_{in}$  is the initial value at the jet exiting station (taken here as 100 times the value of the linear viscosity coefficient at that location).

In region II, linear variation (with respect to the indexing parameter  $i$ ) for the values between the last "ray" in region I and the first ray of region III. This was used to avoid sudden change in the  $\epsilon$ -value, and also to cover the region of possible flow separation, where the proper turbulence model is still needed to be investigated.

The second composite model of sketch B of Figure (2) was also used, but its results are not presented here. No major differences were observed in the results using these two models. In this case, region III of model A is split further into two separate regions, III and IV. In the new region III, a model similar to that of Reference (14) is used with minor alteration. In the present work the model used was

$$\epsilon_{III} = \frac{1}{RT} \frac{b}{\alpha} |u_{i,j} - u_{CL,j}|$$

where

- b is the "width" of the mixing region as shown in Figure (2)
- RT is the Turbulent Reynolds Number taken here as  $(390. - 333. e^{-(.495 M_{i,j})})$
- $u_{CL,j}$  is the  $u$ -velocity at the center line at the point with the index  $j$
- $\alpha$  is a factor for axisymmetry effects



An  $\alpha$  value of 3.0 was found appropriate for the present case. Finally, the value of  $\epsilon$  in region IV was set to zero, representing the inviscid case region. The value of  $\epsilon$  in region II was also taken as the linear interpolation between the values of regions I and III as described previously.

## 5. BOUNDARY CONDITIONS

The conditions on the boundaries of the physical domain, and the corresponding computational domain are shown in Figure (3), and they are discussed next.

### The Incoming Flow Conditions at Station $x = 0$ ( $\xi = 0$ )

The Mach number and all the flow variables are not known at this station, therefore some engineering judgement was required bearing in mind the major objectives of the present work, as stated earlier. It is assumed that the Mach number is still 1.5 at the end of the cylindrical forebody at station 130.47 inches, i.e. that the compression effect at the nose tip is exactly offset by the expansion at the forebody shoulder (see Reference (6) for the details of the test model configuration). Moreover, since computations for the curved boattail start at station 6.49 inches down from station 130.47 inches, the use of the value  $M = 1.5$  is not representative of the real flow. In fact, the tangential Mach number at the station  $x = 0$  was taken as 1.74 based on a Prandtl-Meyer expansion for a  $7^\circ$  turning angle for the corresponding 2-D flow.

The U and V velocity components were then computed at this station knowing the slope of the body at this location. The turbulent profile for the tangential velocity was assumed to be of the  $(1/7)$  power profile, with the boundary layer thickness estimated as 1.12 inches.

The static temperature and pressure profiles were assumed uniform along that boundary, with values of  $0.905 T_{\infty e}$  and  $0.7 P_{\infty e}$  respectively corresponding to the  $7^\circ$  expansion turn.

The density, the specific total internal energy  $e$ , and the eddy viscosity profiles were then computed (using the equation of state, the definition of  $e$ , and the two layer turbulence model) and imposed as the boundary values.

Conditions on the Symmetry Line  $r = 0$  ( $\xi = 1.0$ )

Due to the symmetry, the derivatives in the direction normal to the center line was taken to be zero for certain variables. Since not all the variables should be extrapolated to the axis of symmetry in this manner, otherwise inconsistency and overspecification would result, the following sequence was followed:

- a)  $\frac{\partial(\rho e)}{\partial \xi}$ ,  $\frac{\partial \rho}{\partial \xi}$ ,  $\frac{\partial u}{\partial \xi}$ ,  $\frac{\partial \varepsilon}{\partial \xi}$ ,  $v$  and  $(\rho v)$  were set to zero, then
- b)  $P$  was computed from the equation of state using  $\rho$  and  $e$ , then
- c)  $\rho u$  was computed using  $\rho$  and  $u$ .

Conditions on the Far-Field Boundary ( $\eta = 1.0$ )

The variation along the  $\xi = \text{constant}$  lines near  $\eta = 1.0$  was assumed to vanish. Therefore, the following conditions were applied:

- a)  $\frac{\partial(\rho e)}{\partial \eta}$ ,  $\frac{\partial \rho}{\partial \eta}$ ,  $\frac{\partial u}{\partial \eta}$ ,  $\frac{\partial \varepsilon}{\partial \eta}$  and  $\frac{\partial v}{\partial \eta}$  were set to zero, then
- b)  $P$  was computed from the equation of state using  $\rho$  and  $e$ , then
- c)  $\rho u$  and  $\rho v$  were computed using  $\rho$ ,  $u$  and  $v$ .

Conditions at the Wall and at the Nozzle Exit ( $\eta = 0.0$ )

On the boattail wall:

a)  $u$  and  $v$  are zero for no slip, then  $(\rho u)$ ,  $(\rho v)$  and also  $\varepsilon$  are zero.  $T$  is set at  $T_w$ , taken equal to the stagnation temperature of the external free stream  $T_{0e}$ , to simulate the wind tunnel tests or  $T_w$  can be specified independently for hot wall cases

- b)  $\frac{\partial P}{\partial \eta}$  is set to zero, then
- c)  $p$  is computed from the equation of state utilizing  $P$  and  $T$ , then
- d)  $(\rho e)$  is computed using  $\rho$ ,  $u$ ,  $v$  and  $T$

### For the Nozzle Exit Plane

a) Uniform profiles  $u = u_j$ ,  $T = T_j$ ,  $P = P_j$  and  $v = 0$  were imposed, where  $u_j$ ,  $T_j$ ,  $P_j$  are computed from the given experimental conditions for  $T_{0j}$ ,  $P_{0j}$ ,  $Re_j$  and assuming exit Mach number of 1.01.  $Re_j$  is the jet Reynolds number which was varied in the experiments to yield the required NPR.

b)  $\rho$  is computed from the equation of state, and  $\epsilon$  at this boundary was estimated as  $(100 \mu_j)$

c)  $(\rho u)$ ,  $(\rho v)$  and  $(\rho e)$  were then computed using  $\rho$ ,  $u$ ,  $v$  and  $T$ .

The  $u$  velocity at the first grid point in the jet flow nearest to the inner nozzle surface was set to  $0.5 u_j$  to reflect the effect of viscosity and simulate the corresponding very thin boundary layer<sup>15</sup>.

As mentioned previously, a smooth curve was used to join the points AB in Figure (2.8), instead of the vertical line AC. This will not be of any major consequence regarding the correct location for placing the correct boundary conditions, if

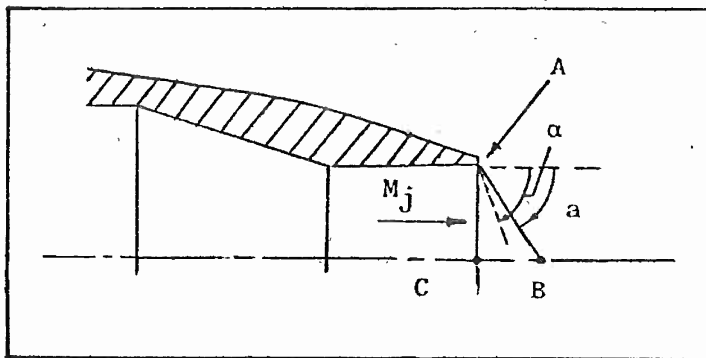


Figure 9. Boundary Conditions Placement for the Jet Flow.

the line AB is a characteristic line for the supersonic jet. Then, according to the linear inviscid supersonic theory, the flow conditions at line AC remain the same and equal to those at line AB. With the nozzle assumed in choking condition,  $M_j$  was taken 1.01 with a corresponding characteristic angle  $\alpha = 81.9^\circ$ . However, line AB was taken at another angle  $a = 74^\circ$  for smooth curvature. This difference in location is not expected to affect the solution considerably, especially if one considers the objectives of the present work.

Although the smooth shoulder line was essential for obtaining successful solutions, its geometry is not expected to influence the gate this behavior.

### SECTION III

#### THE NUMERICAL PROCEDURE

The time-dependent, predictor-corrector MacCormack's explicit scheme<sup>16-18</sup> is used to solve Equation (2.8) as successive enhancement in time toward the steady state flow solution.

#### 1. SPLITTING PROCEDURE

The solution is obtained by two-step splitting in the  $\eta$ - and  $\xi$ - directions. Solution advancement in time can start in the  $\eta$ - and then the  $\xi$ - direction or vice versa, depending on which is larger,  $\Delta t_\eta$  or  $\Delta t_\xi$  (as defined and estimated in Section (3.2)).

The operator  $L_\xi(\Delta t_\xi)$  denotes the enhancement of the solution of

$$\frac{\partial U}{\partial t} + \xi_x \frac{\partial F}{\partial \xi} + \frac{1}{j_o} \xi_r \frac{\partial (r_o^j G)}{\partial \xi} = 0 \quad (3.1a)$$

in the  $\xi$ -direction by time increment of  $\Delta t_\xi$  seconds. Similarly,  $L_\eta(\Delta t_\eta)$  represents the similar meaning for the enhancement of the solution of

$$\frac{\partial U}{\partial t} + \eta_x \frac{\partial F}{\partial \eta} + \frac{1}{j_o} \eta_r \frac{\partial (r_o^j G)}{\partial \eta} = j_o \cdot \frac{H}{j_o} \quad (3.1a)$$

in the  $\eta$ -direction by  $\Delta t_\eta$  increment.

The dependent vector variable  $U(\eta, \xi, t)$  was then advanced in time as:

$$U(\eta, \xi, \Delta t) = [L_\xi^{M/2}(\Delta t_\xi/2) L_\eta(M\Delta t_\xi) L_\xi^{M/2}(\Delta t_\xi/2)] \cdot U(\eta, \xi, t)$$

with  $\Delta t = M\Delta t_\xi$  if  $\Delta t_\xi < \Delta t_\eta$

or as

$$U(\eta, \xi, \Delta t) = [L_\eta^{N/2}(\Delta t_\eta/2) L_\xi(N\Delta t_\eta) L_\eta^{N/2}(\Delta t_\eta/2)] \cdot U(\eta, \xi, t)$$

with  $\Delta t = N\Delta t_\eta$  if  $\Delta t_\eta < \Delta t_\xi$

(3.2a,b)

where M and N are the smallest even integers of the quotients  $\Delta t_\eta / \Delta t_\xi$  and  $\Delta t_\xi / \Delta t_\eta$ , respectively and  $\Delta t_\eta$ ,  $\Delta t_\xi$  are the maximum allowable time steps in the  $\eta$  and  $\xi$  directions as determined by the Courant-Friedrichs-Lewy (CFL) limit with viscous stability requirement as will be shown and given by Equation (3.3).

The values of M and N were chosen to be close to 2 for the present work by changing the grid distribution. This fact allows a truly alternating direction procedure and is favored for the present set of coordinates to enforce the boundary conditions (especially at the jet exit plane) through frequent alternation. The present case is dissimilar to the simple flat plate case where one direction (the streamwise) has very little gradients and the need for frequent alternation of the solution path is unnecessary.

The maximum time step as determined by the CFL condition is not necessarily very near the wall, but rather in the viscous mixing region. In addition, the ratio  $(\Delta t_\eta / \Delta t_\xi)$  can change drastically from less to greater than 1.0 depending upon the relative flow conditions of the external flow to the jet flow, as was noticed for the different flow case considered. Therefore, form 3.2a or b can then be selected accordingly. This procedure was automated in the computer program.

## 2. STABILITY CONDITION, ESTIMATED MAXIMUM TIME STEP

The numerical stability requirement for MacCormack's explicit scheme is governed by the (CFL) conditions expressed in the case of Cartesian coordinates<sup>17</sup> as:

$$\Delta t = \underset{i,j}{\text{minimum}} (\Delta t_x; \Delta t_y)$$

$$= \underset{i,j}{\text{minimum}} \left[ \frac{\Delta x}{|u_{i,j}| + c_{i,j} + \max \left\{ \frac{2\gamma}{\rho} \left( \frac{\mu}{P_r} + \frac{\epsilon}{P_{r_t}} \right) \frac{1}{\Delta x}, \frac{\sqrt{-\lambda_t (\mu + \epsilon)}}{\Delta y} \right\}}; \right.$$

$$\left. \frac{\Delta y}{|v_{i,j}| + c_{i,j} + \max \left\{ \frac{2\gamma}{\rho} \left( \frac{\mu}{P_r} + \frac{\epsilon}{P_{r_t}} \right) \frac{1}{\Delta y}, \frac{\sqrt{-\lambda_t (\mu + \epsilon)}}{\Delta x} \right\}} \right]$$

In the present case,  
an estimate for the  
maximum time step was  
calculated as:

$$\Delta t = \text{minimum}_{i,j} (\Delta t_{\eta}; \Delta t_{\xi})$$

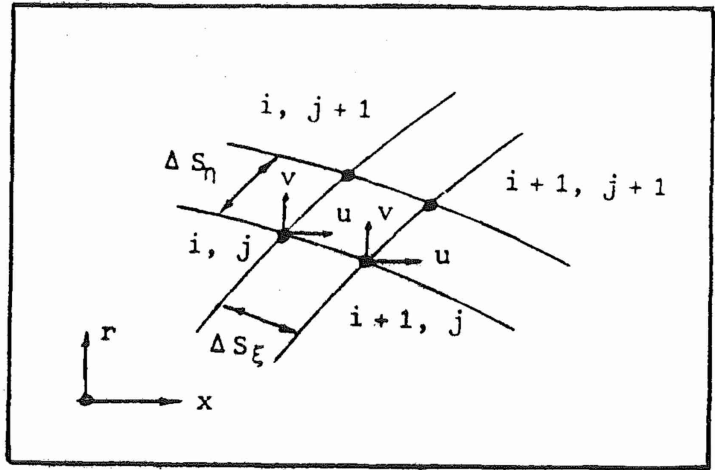


Figure 10. Nomenclature for  
Estimating the Maximum  
Time Step.

where

$$\Delta t_{\eta} = \text{minimum} \left[ \frac{\Delta S_{\eta}}{|u_{\eta}| + c} \right]_{i,j}; \frac{\Delta S_{\eta}}{\max \left\{ \frac{2\gamma}{\rho} \left( \frac{\mu}{P_r} + \frac{\epsilon}{P_{r_t}} \right) \frac{1}{\Delta S_{\eta}}, \sqrt{\frac{-\lambda_t(\mu + \epsilon)}{\Delta S_{\xi}}} \right\}} \quad (3.3a)$$

and

$$\Delta t_{\xi} = \text{minimum} \left[ \frac{\Delta S_{\xi}}{|u_{\xi}| + c} \right]_{i,j}; \frac{\Delta S_{\xi}}{\max \left\{ \frac{2\gamma}{\rho} \left( \frac{\mu}{P_r} + \frac{\epsilon}{P_{r_t}} \right) \frac{1}{\Delta S_{\xi}}, \sqrt{\frac{-\lambda_t(\mu + \epsilon)}{\Delta S_{\eta}}} \right\}} \quad (3.3b)$$

where

$$\Delta S_{\xi} = \sqrt{(x_{i,j} - x_{i-1,j})^2 + (r_{i,j} - r_{i-1,j})^2},$$

$$\Delta S_{\eta} = \sqrt{(x_{i,j} - x_{i,j-1})^2 + (r_{i,j} - r_{i,j-1})^2},$$

$$u_{\xi} = \text{Max. } (u_{i,j}, v_{i,j}, u_{i-1,j}, v_{i-1,j}),$$

and

$$u_{\eta} = \text{Max. } (u_{i,j}, v_{i,j}, u_{i,j-1}, v_{i,j-1})$$

The actual time step finally used was less than this estimated maximum. A factor of 0.7 was used.

### 3. NUMERICAL DAMPING

The fourth order pressure gradient damping concept as introduced by MacCormack and Baldwin<sup>17</sup> is applied here, though in slightly different form to suit the present case. The constant  $\alpha_0 = 0.5$  for the flat plate case as used in that reference, for example, has now been made a function of the location (space). It was also logical to correlate this function to the coordinate transformation derivatives  $\eta_x$ ,  $\eta_r$ ,  $\xi_x$  and  $\xi_r$ .

This damping was applied in both computational sweeps in the  $\eta$ - and  $\xi$ - directions. Some numerical experimentation led to the choice of the eight constants introduced in front of the transformation coefficients to allow local control on the damping in the present coordinates.

This damping is implemented by replacing

$$F_{ii,j} \text{ by } F_{ii,j} + F_{D_{ii,j}}$$

and

$$G_{ii,j} \text{ by } G_{ii,j} + G_{D_{ii,j}}$$

in both the predictor and corrector steps of the  $\xi$ -solution sweep of Equation (3.1a). Here,  $ii = i$  and  $i + 1$  for the predictor and the corrector steps, respectively.

The following expressions for  $F_D$  and  $G_D$  were used

$$F_{D_{ii,j}} = C_{\xi 1} (|u_{ii,j}| + c_{ii,j}), \frac{|P_{i+1,j} - 2P_{i,j} + P_{i-1,j}|}{(P_{i+1,j} + 2P_{i,j} + P_{i-1,j})}$$

$$G_{D_{ii,j}} = C_{\eta 1} (|v_{ii,j}| + c_{ii,j}), \frac{|P_{ii,j+1} - 2P_{ii,j} + P_{ii,j-1}|}{(P_{ii,j+1} + 2P_{ii,j} + P_{ii,j-1})}$$

where

$$C_{\xi 1} = 0.02 \xi_{x_{ii,j}}^2 + 0.12 \xi_{r_{ii,j}}^2$$

$$C_{\eta 1} = 0.01 \eta_{r_{ii,j}}^2 + 0.09 \eta_{x_{ii,j}}^2$$

Then, in the  $\eta$ -sweep, the same procedure is similarly implemented by replacing

$$F_{i,jj} \text{ by } F_{i,jj} + F_{D_{i,jj}}$$

and

$$G_{i,jj} \text{ by } G_{i,jj} + G_{D_{i,jj}}$$

where

$$F_{D_{i,jj}} = C_{\xi_2} (|u_{i,jj}| + c_{i,jj}) \frac{|P_{i+1,jj} - 2P_{i,jj} + P_{i-1,jj}|}{(P_{i+1,jj} + 2P_{i,jj} + P_{i-1,jj})}$$

and

$$G_{D_{i,jj}} = C_{\eta_2} (|v_{i,jj}| + c_{i,jj}) \frac{|P_{i,j+1} - 2P_{i,j} + P_{i,j-1}|}{(P_{i,j+1} + 2P_{i,j} + P_{i,j-1})}$$

where

$$C_{\xi_2} = 0.02 \xi_x^2(i,jj) + 0.09 \xi_r^2(i,jj)$$

$$C_{\eta_2} = 0.10 \eta_r^2(i,jj) + 0.02 \eta_x^2(i,jj)$$

where  $jj=j$  and  $j+1$  for the predictor and corrector steps, respectively and  $c_{i,j}$  is the local speed of sound.

It can be shown that this damping will give rise to fourth order terms in the form:

$$C_{\xi_1} \Delta t \Delta \xi^3 \frac{\partial}{\partial \xi} \left[ \frac{|u|+c}{4P} \frac{\partial^2 P}{\partial \xi^2} \cdot \frac{\partial U}{\partial \xi} \right] + C_{\eta_1} \Delta t \Delta \eta^3 \frac{\partial}{\partial \eta} \left[ \frac{|v|+c}{4P} \frac{\partial^2 P}{\partial \eta^2} \cdot \frac{\partial U}{\partial \eta} \right]$$

in the  $\xi$ -direction, and

$$C_{\eta_2} \Delta t \Delta \eta^3 \frac{\partial}{\partial \eta} \left[ \frac{|v|+c}{4P} \frac{\partial^2 P}{\partial \eta^2} \cdot \frac{\partial U}{\partial \eta} \right] + C_{\xi_2} \Delta t \Delta \xi^3 \frac{\partial}{\partial \xi} \left[ \frac{|u|+c}{4P} \frac{\partial^2 P}{\partial \xi^2} \cdot \frac{\partial U}{\partial \xi} \right]$$

in the  $\eta$ -direction.

In addition to this pressure damping, the normal stress damping concept as used by McRea<sup>9</sup> and others was used here. This damping, represented by the factor  $\beta$  in Equation (2.7), affects



directly the normal stresses without affecting the shear stresses. The value of  $\beta = -6$  was used. It is not always possible or recommended to use very large values, at least for the explicit schemes, since it directly decreases the allowable time steps, through  $\lambda_t$ , as can be noticed from Equation (3.3). It is preferable to remove  $\beta$  when convergence is almost achieved to eliminate additional changes to the original Navier-Stokes equations.

#### 4. IMPLEMENTATION OF THE BOUNDARY CONDITIONS

It is noted here that the steady state boundary conditions for the time dependent equations are imposed for both parts (Equation (3.1)) of the original governing equations.

First-order accurate, two-point extrapolation was used to compute the value of the variables at the wall, far-field boundary and the axis of symmetry for the derivative-type conditions. Although arguments may arise concerning the need for use of three-point, second-order accurate forms to keep the numerical scheme totally second-order accurate, it was experienced<sup>19</sup> that this leads to instability in some cases. Further, the use of a two-point formula is more consistent with MacCormack's basic two-point, two-step scheme.

In addition, it was found essential during the early time-evolvment of a solution to fix the density at the point I=27 (Figure 2.5b). The reason for that is that the pressure at point I=27 is relatively low in the low pressure pocket in the nozzle lip region, relative to the value at point I=28 (in the jet). Therefore, instead of fixing the pressure at this point (I=27), the density was instead fixed to influence the continuity relation and the energy equations, thus influencing the solution more significantly. The average value for points I=26 and 28 was assigned to the point I=27. This procedure was maintained until the solution stabilized and then it was lifted without difficulty. However, obtaining a solution was not possible without such procedure, due to blow up in the solution due to negative pressure values occurring in this low pressure region during early stages of convergence.

## 5. INITIAL CONDITIONS

Since signals can only affect downstream flow computations in supersonic flow cases (along lines of characteristics and within the zone of influence), it was anticipated that the incoming flow profiles at the starting station will strongly affect the solution in the whole domain. Therefore, the initial conditions were based on that profile.

These initial values are not the most adequate near the jet exit station, but the boundary conditions at this location are expected at the supersonic speed of the jet to influence the solution in this location immediately in time.

It was noticed that starting with a solution that allows the flow specified by the incoming profiles to expand rather than to recompress helps in obtaining quicker convergent solution and reduces numerical instability. It is suggested that if no appropriate starting solution can be established, then starting with low-level values everywhere may be more adequate for the supersonic flow cases.

SECTION IV  
RESULTS AND DISCUSSION

1. DATA OF EXPERIMENTS AND THE CASES COMPUTED

A total of five different cases were computed. Four cases were run for the specific nozzle boattail under consideration (the AGARD 10°-nozzle) and one case for a similar AEDC model, with cold jet exhaust to study the effect of the nozzle boattail geometry.

The experimental results<sup>6</sup> of the base case with the cold exhaust were obtained under the following test conditions for the external flow:

$$M_{\infty e} = 1.5, \quad T_{oe} = 580^\circ\text{R}, \quad Re_e = 2.5 \times 10^6/\text{ft}$$

with the jet exhaust being under the conditions:

$$T_{oj} = 540^\circ\text{R}, \quad RT \text{ (Throat Reynolds Number)} = 1.773 \times 10^6, \\ \text{nozzle exit diameter} = 3.982 \text{ inches.}$$

These conditions for the jet flow will yield a nozzle pressure ratio NPR of 7.09, where NPR is defined as  $P_{oj}/P_{\infty e}$ . However, the ratio  $P_j/P_{\infty e}$  is only 3.746.

The following conditions can then be computed for the external flow:

$$U_{\infty e} = 1470.4 \text{ ft/sec}, \quad T_{\infty e} = 400^\circ\text{R} \\ P_{\infty e} = 354.1 \text{ lb/ft}^2, \quad P_{oe} = 1300 \text{ lb/ft}^2$$

Also, for the jet flow one can compute:

$$U_j = 1040.6 \text{ ft/sec}, \quad T_j = 450^\circ\text{R} \\ P_{oj} = 2510 \text{ lb/ft}^2, \quad P_j = 1324.6 \text{ lb/ft}^2$$

The hot exhaust case was computed with  $T_{oj} = 2100^\circ\text{R}$  and the hot boattail wall case was computed for  $T_w = 1100^\circ\text{R}$ . The exit conditions for the hot exhaust can then be computed as:

$$\begin{aligned} U_j &= 2052.1 \text{ ft/sec} & , & & T_j &= 1749.4^\circ\text{R} \\ P_{oj} &= 2510 \text{ lb/ft}^2 & , & & P_j &= 1324.6 \text{ lb/ft}^2 \end{aligned}$$

Finally, the corresponding 2-D case and AEDC nozzle model case were computed for cold exhaust temperature as in the base case.

## 2. COMPUTATION DETAILS

All the computations were run on the CDC-6600 computer with a mesh of  $30 \times 39$  points in the  $\eta$ - $\xi$  plane with  $\Delta\eta = 0.03448$  and  $\Delta\xi = 0.0263$ .

Computations were expected to last until the accumulative physical time reaches at least  $4t_{ch}$  where  $t_{ch} = L/U_{\infty e} = 12.9 \times 10^{-4}$  second, where  $L$  is the length of the physical computation region, here as 26.0 inches. The convergence criterion was based on the condition that the maximum change in the static pressure over one  $t_{ch}$  should be less than five percent. Only the first case with the AEDC nozzle geometry, with initial conditions as prescribed earlier, was left to exceed  $8t_{ch}$  and the  $c_p$  at the boattail surface was monitored. The values of  $c_p$  at different times are shown in Figure (4.1).

The largest changes observed were usually in the static pressure and particularly along the center line  $r = 0$ . For the base case of cold exhaust for the AGARD nozzle, the maximum change in the pressure along the center line was 4.5 percent along the time interval  $t = 4 t_{ch}$  to  $t = 5.9 t_{ch}$ .

For other cases, computations were stopped after about  $t \approx 4 t_{ch}$ , by making use of the computed case of cold exhaust as the starting initial conditions, thus also eliminating most of the numerical difficulties and achieving faster convergence rates.

The computation time for the typical base case was 0.022 sec/grid point per cycle per one  $t_{ch}$ . Cycle here denotes three sweeps: two in the  $\eta$ -direction and one in the  $\xi$ -direction.

This amounts to a large computer time and it is mainly due to the very small allowable time steps for the explicit scheme as required by the stability condition of Equation (3.3). For the base case, this maximum time step was  $0.26 \times 10^{-6}$  sec.

The lengthy computations were made with a restart feature, allowing reasonable computation intervals and continuation according to the computer resources available. However, implicit or hybrid schemes are strongly recommended for study and possible successful applications to the present flow case.

### 3. COMPARISON WITH THE EXPERIMENT

The computer code was first validated by comparing with the experimental results of Reference (6), where the surface pressure coefficient is provided for the cold exhaust case at the present Mach number of 1.5 .

Figure (4) shows the computed pressure coefficient  $c_p = (P_w - P_{\infty e}) / (1/2 \rho_{\infty e} U_{\infty e}^2)$ , compared with the experimental measurements for the upper and lower locations. The recompression seems to be weaker than that measured, and the agreement does not seem to be excellent, resulting in estimated pressure drag higher than the experimental value. It can also be seen that the smaller  $c_p$  computed near  $x = 0$  is mainly due to the imposed pressure profile.

The main reason for the present deviation is that the flow pattern ceases to be axisymmetric during experimentation due to the effect of the model support. The flow turns into a truly three-dimensional flow with strong swirling cross flow, while computation models true axisymmetry. The present results however, are better than any known for supersonic flow at this relatively high nozzle pressure ratio. The results of Reference (2), for example, agree well with the corresponding experiment only for subsonic flow up to  $M_{\infty e} = 0.9$  and NPR up to 2.95 but quickly deteriorate for supersonic flow at  $M_{\infty e} = 1.1$  and NPR = 4.77. It is also expected to deteriorate more at the present conditions of  $M_{\infty e} = 1.5$  and NPR of 7.09 .

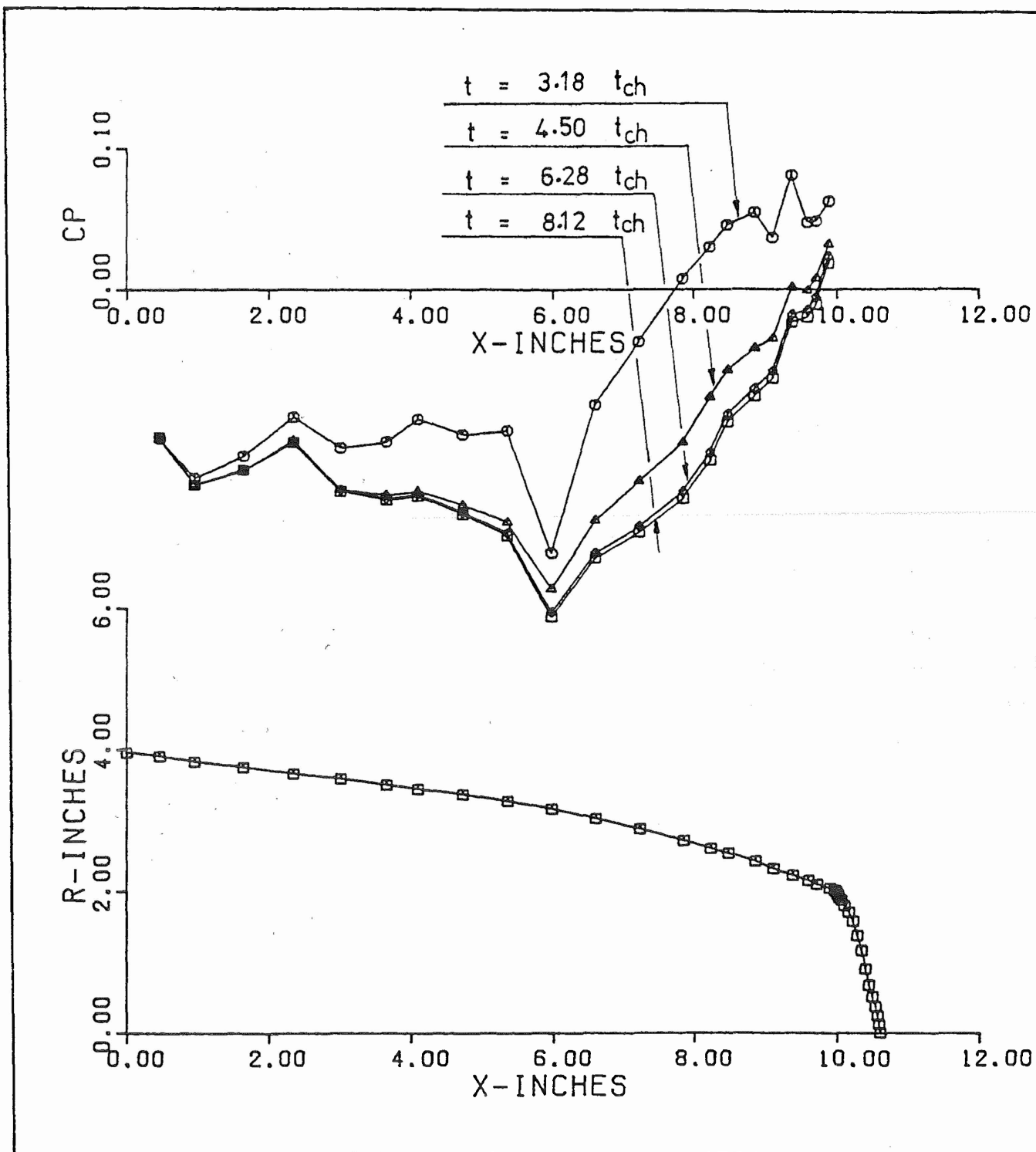


Figure 11a. Development of the Surface Pressure Coefficient.

Details of the flow field for this base case can be seen in Figures 9A, 10A, 11A and 12A. From the Mach line contours of Figure 9A, it can be seen that the subsonic region protrudes considerably down stream of the nozzle. No reversed flow region was detected for this case, as was also confirmed by the experiment as indicated in Reference (6). In fact, no reversed flow regions were reported<sup>10</sup> for the 10° and 15° nozzle tested with NPR up to 15.8 .

Another useful result is the static temperature distribution which is essential for the infrared signature analysis of the jet exhaust plume. The static temperature contours are shown in Figure (10A) where the jet temperature drops due to the expansion, then increases when the recompression starts. It is also noticeable the effect of the discontinuity of the surface temperature boundary condition where  $T_w = 580^\circ\text{R}$  on the boattail surface, while the jet exhaust static temperature is  $450^\circ\text{R}$ .

The flow pattern of the exhaust plume is of the repeated weak reflection system. The pressure and the u-velocity along the centerline of the jet are shown in Figure (4.2) where the values are normalized by the value at the starting station at  $i = 1$ . The flow expands to a low pressure at B and the reflected expansion wave at the plume surface reflects as compression wave (Figure (1.1A)) causing the pressure to increase in the region BC. Then it starts to drop in region CD due to the expansion suffered from the reflected shock that is reflected again at the plume boundary as an expansion wave. It is interesting to notice the change in the velocity component along the axis of symmetry.

#### 4. BOATTAIL GEOMETRY EFFECTS

The effect of the boattail geometry on the pressure drag is of practical concern for jet engine designers. Optimizing the boattail geometry to give minimum drag is usually a major factor. Therefore, another nozzle geometry case (the AEDC nozzle) was computed. The pressure coefficients for both geometries are shown in Figure (5), where the AGARD nozzle shows smaller  $c_p$ . However,

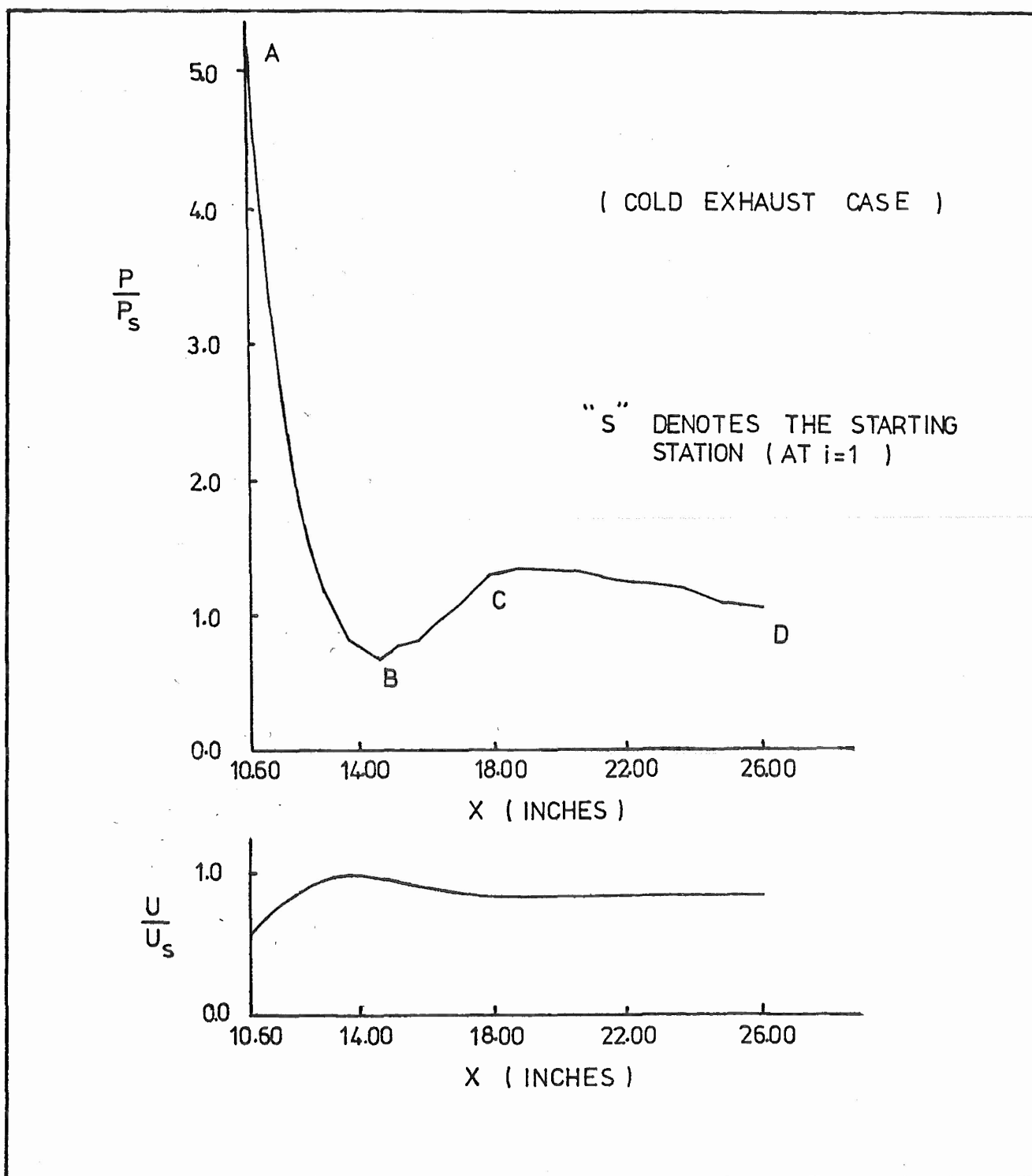


Figure 11b. Axial Variation in  $u$  and  $P$ .



when computing the pressure drag for both the geometries, they were almost equal, thus giving the AGARD nozzle the advantage due to the larger wetted surface. The "kink" observed at  $x \approx 2.2$  inches for the AEDC model lacks reasonable explanation.

The flow pattern, in general, was similar to the AGARD nozzle case with no major differences.

## 5. HOT EXHAUST EFFECTS

The effect of the hot exhaust is propagated upstream to the boattail surface through the subsonic region of the boundary layer. The pressure coefficient for this case was smaller than the corresponding cold exhaust case as can be seen in the middle curves of Figure (6). Although the difference seems to be small and the curves seem to be slightly shifted upward, the computed pressure drag was considerably smaller for the hot exhaust case by the ratio of 79% in comparison with the cold exhaust case. This is quite important if we consider the exhaust temperature ratio as  $T_{Oj}(\text{hot})/T_{Oj}(\text{cold}) = 3.89$ .

The mixing of the hot jet with the outer stream is presented by Figures (11A, 12A). The static temperature profiles for both the cold and hot exhausts normalized by the corresponding jet static temperature, are shown in Figure (11A). The symbol  $j$  represents the point location index on the axis of symmetry. At the location  $j = 30$ , which marks the location of the far-field boundary (at a distance of four times the jet exit diameter), the static temperature  $= 0.66 T_j(\text{hot})$  and also  $= 2.90 T_{\infty e}$ . For the cold exhaust, the temperature at that location is  $0.77 T_j$  and  $= 0.87 T_{\infty e}$ . It is obvious, and expected, that the hot exhaust plume needs longer distance to attain free stream temperature value.

The mixing in the axial velocity component is shown in Figure (12A). At the same location of  $j = 30$ , the velocity is  $u = 1.15 U_j$  and  $= 1.61 U_{\infty e}$  for the hot jet. The corresponding values are  $u = 1.47 U_j$  and  $= 1.04 U_{\infty e}$  for the cold jet. The

same remark about longer distance along the axis of symmetry to attain the external free stream conditions holds for the axial velocity component for the hot exhaust.

It is then appropriate to observe the changes in the velocity, temperature and pressure along the axis of symmetry for this particular case of practical importance. This is given by Figure (7), where it is clear that the high static pressure of the jet drops quickly to match the "surrounding" low pressure condition. However, it seems that the axial velocity and the static temperature will take longer distances to get in equilibrium with the corresponding external flow conditions.

Finally, the density contours for the hot exhaust are shown in Figure (8). It was always noticed that the velocity components and the static temperature had smooth profiles, while the density and consequently the static pressure (computed from the equation of state, using  $\rho$  and  $T$ ) had local irregularities in their contours and profiles. This might be explained as a consequence of having either excess or less than enough pressure damping as described in Section (3.3). Another explanation is that the density is computed from the first order continuity equation, with one boundary condition to enforce. In addition, the transformation derivatives were not totally smooth due to the specific coordinates used and the many requirements imposed on them. These irregularities in the derivatives are expected to be reflected in the obtained solution, however this does not explain the smoothness in the velocities. Figure (8) is a good example for the irregularities in the density contours, which also bears the additional effects due to the linear interpolation used for contour plotting in addition to the effect of large grid mesh.

## 6. BOATTAIL SURFACE TEMPERATURE EFFECTS

In addition to the low temperature case of  $T_w = 580^\circ\text{R}$ , a case with  $T_w = 1100^\circ\text{R}$  was computed and the pressure coefficients for both cases are displayed at the top of Figure (6). The

pressure coefficient is much smaller for the hot wall case and the drag is 67% of the corresponding cold wall value. The irregularities in  $c_p$  curve near  $x \approx 10$  inches is partially due to the effect of the discontinuity in "wall" temperature between wall and the exiting jet.

It is of interest to see the effect of the wall temperature on the static temperature field. This can be studied from Figure (10B) where the changes, as might be expected, are only confined to the surface region. Otherwise, the same pattern exists as compared with the cold wall case (the base case) of Figure (10A).

The velocity flow field for this case was plotted in Figure (13A) where the direction of the arrows represents the flow directions. However, the stream lines cannot be traced properly by the arrows. Therefore, the corresponding stream lines were computed by direct integration and contours of the streamlines are shown in Figure (13B). No separation bubbles were detected as stated before. Also, a mass conservation was made to compute the diameter of the jet tube. For the jet exiting from an exit radius of 3.982 inches, conservation of mass showed that this radius increases to 6.510 inches, i.e. 163 % for this case.

## 7. THE TWO-DIMENSIONAL CASE

A two-dimensional model for the AGARD 10°-nozzle axisymmetric case was computed by minor changes in the code, mainly by setting  $j_0 = 0$  instead of 1 in the Equation (2.8). The pressure coefficient is plotted at the bottom of Figure (6) with comparison with the axisymmetric case. The pressure coefficient for this case is larger than the axisymmetric case before the recompression at  $x \approx 6$  inches and smaller after the recompression. It is surprising that the recompression occurs at almost the same location for all of the cases considered. This location seems to be more dependent on the NPR which is constant for the present cases. There is also unexplainable irregularities near  $x \approx 10.0$  for the two-dimensional case. However, it is expected that the disturbance

due to the two-dimensional geometry to be larger in general and to extend far down stream longer than in the axisymmetric case. This can be best shown by Figure (9) for the Mach line contours. The sonic line, for example, protrudes down stream in the two-dimensional case further than in the axisymmetric case.

SECTION V  
SUMMARY AND RECOMMENDATIONS

1. SUMMARY

It has been shown that complex flow cases can now be computed as a step toward the final goal of computing the flow past a real three-dimensional aircraft model. Finite difference solutions for supersonic flow at Mach number 1.5 past axisymmetric and two-dimensional nozzles with real jet exhaust, were obtained using the complete Navier-Stokes equations. The viscous turbulent mixing between the two flow streams was handled through the present approach, without any assumption or approximation.

The explicit, time dependent, second order accurate MacCormack's scheme was used with the emphasis being on the demonstration of the success of the present unified approach, rather than on emphasizing high accuracy or computational efficiency.

Five different cases were computed and reported<sup>20</sup>, all at nozzle pressure ratio  $P_{0j}/P_{\infty e} = 7.09$  to study the effects of boattail geometry, jet exhaust temperature, boattail surface temperature and the differences between the axisymmetric and two-dimensional cases. The surface pressure coefficient and the pressure drag were the main subject of interest, more than the profile drag (skin friction), due to the unavailability of experimental results for the latter and also to relieve the larger grid point number and the longer computation time that is needed. Comparison with the experiment is reasonable if the three-dimensionality of the experimental results is considered.

The hot exhaust case yielded a smaller pressure drag, 79% of the corresponding drag for the cold exhaust case. The hot boattail surface case yielded a smaller pressure drag, 67% of the same corresponding cold wall case. The computation, assuming axisymmetry gave larger pressure drag than experimentally predicted. The location of the recompression on the boattail surface was not changed in all five cases computed. It is assumed that this location should be a strong function of the nozzle pressure ratio, which was constant in all the cases.

## 2. RECOMMENDATIONS FOR FURTHER STUDIES

For better accuracy, more grid points will be needed for computation if the turbulent profile drag is to be estimated with reasonable accuracy. This will directly increase the computation time to impractical figures, therefore, implicit or hybrid schemes<sup>21,22</sup> should be studied and used, if possible, to avoid the tight stability restriction on explicit schemes.

The normal shock mode (Mach disk mode) for the present flow case has not yet been computed successfully for the higher nozzle pressure ratios. Studies should be made toward establishing the factors that affect such computations (e.g. initial conditions, type of pressure boundary conditions<sup>23</sup>, mesh spacing near and across the disk, different approaches or numerical methods<sup>24</sup>,...). Use of the strong conservation form of the governing equations (Equation 2.9) rather than the weak form (Equation 2.8) might be tested to access the effects on accuracy and possible improvement in shock capturing ability.

The effects of the turbulence eddy viscosity model used on the obtained solutions have not yet been established. Studies for better models are still needed. Also, better and more representative boundary conditions (profiles) at the starting station of computation, would be of direct help for improved results. Such information can be obtained from experiments if in-advance coordination between the experimental and computational efforts are possible. In addition, the effect of the location of the far-field conditions on the solution is still needed to be studied and evaluated.

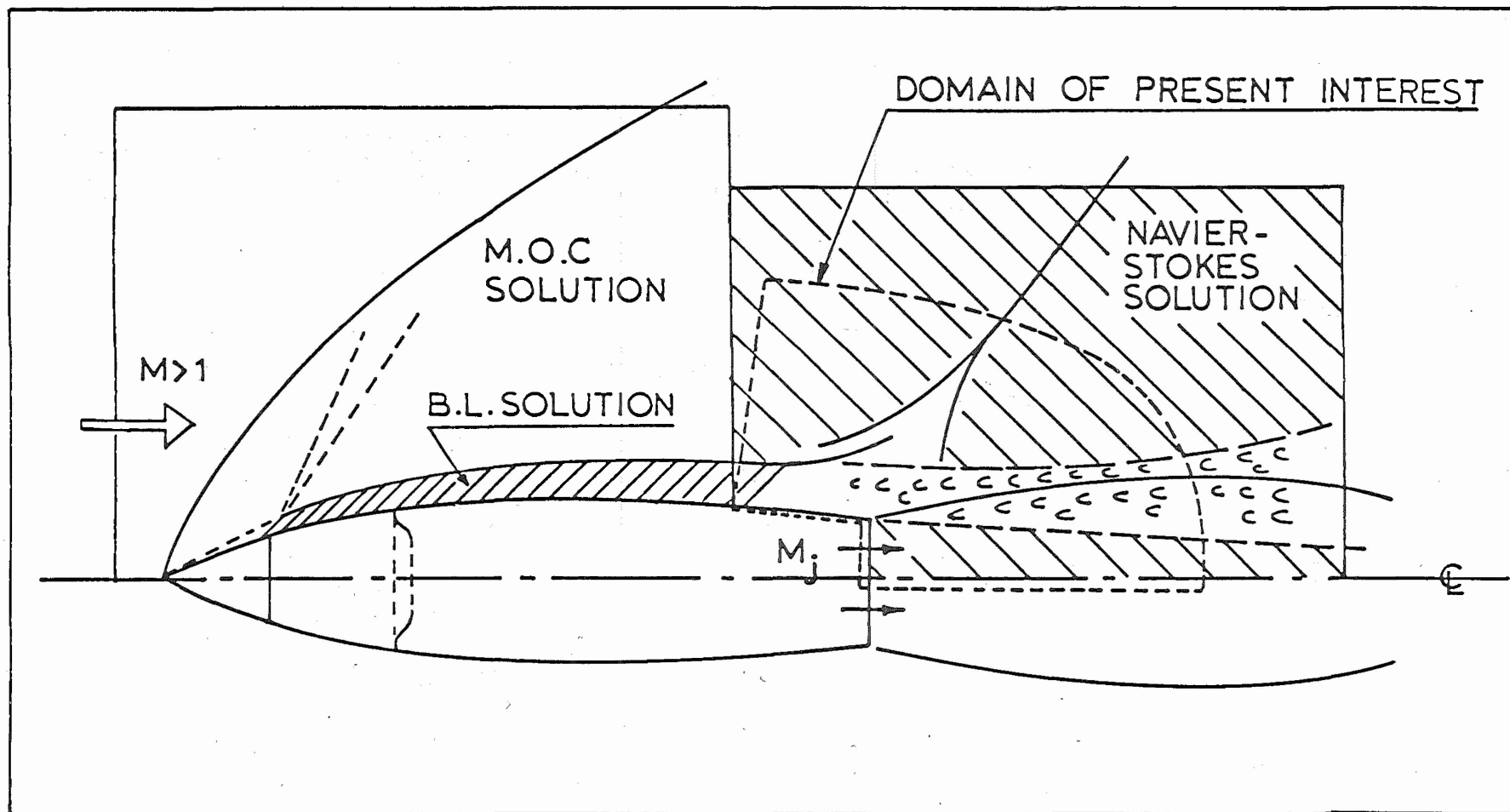


Figure 12. Domain of Present Interest.

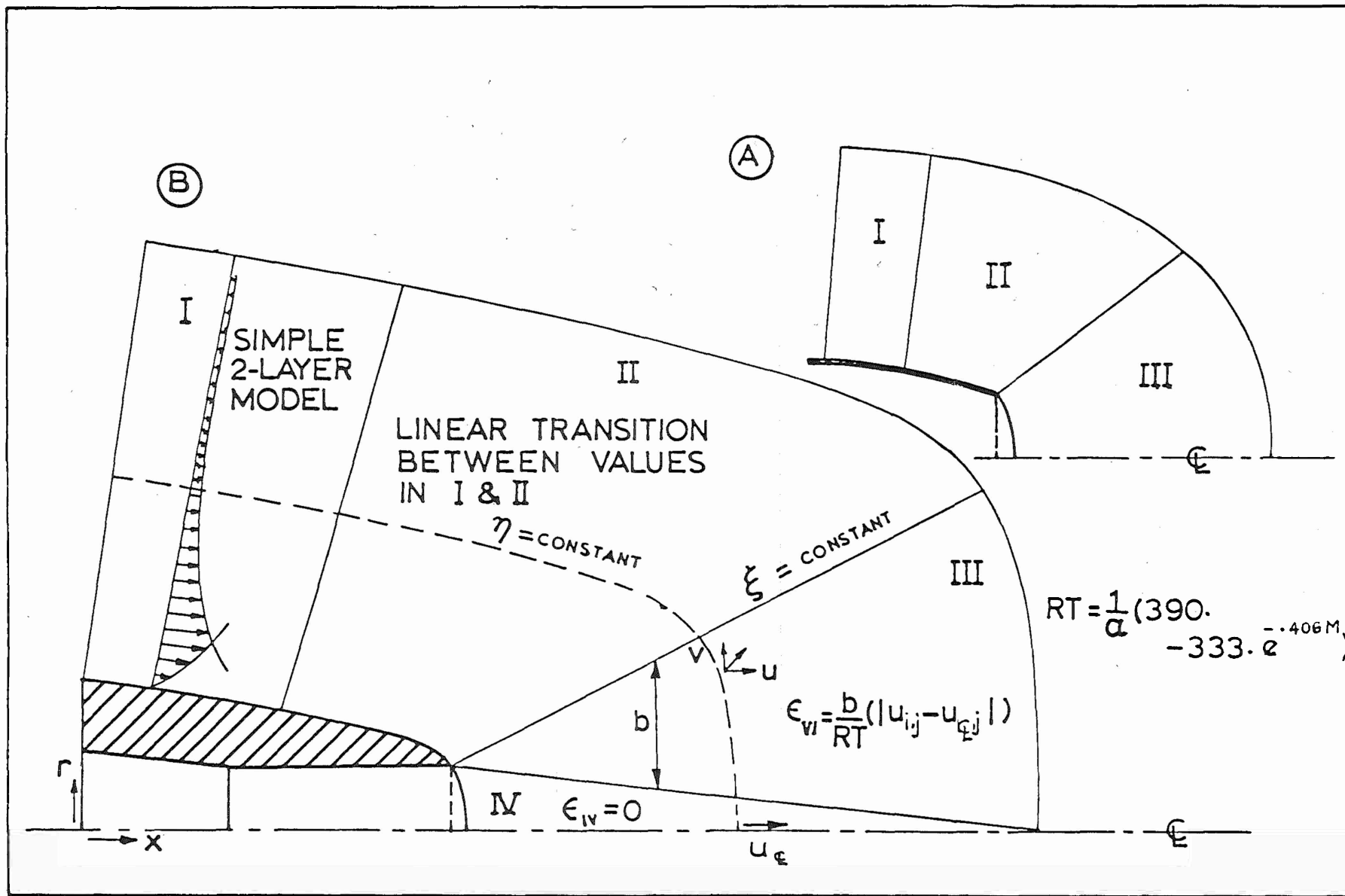


Figure 13. Eddy Viscosity Models.



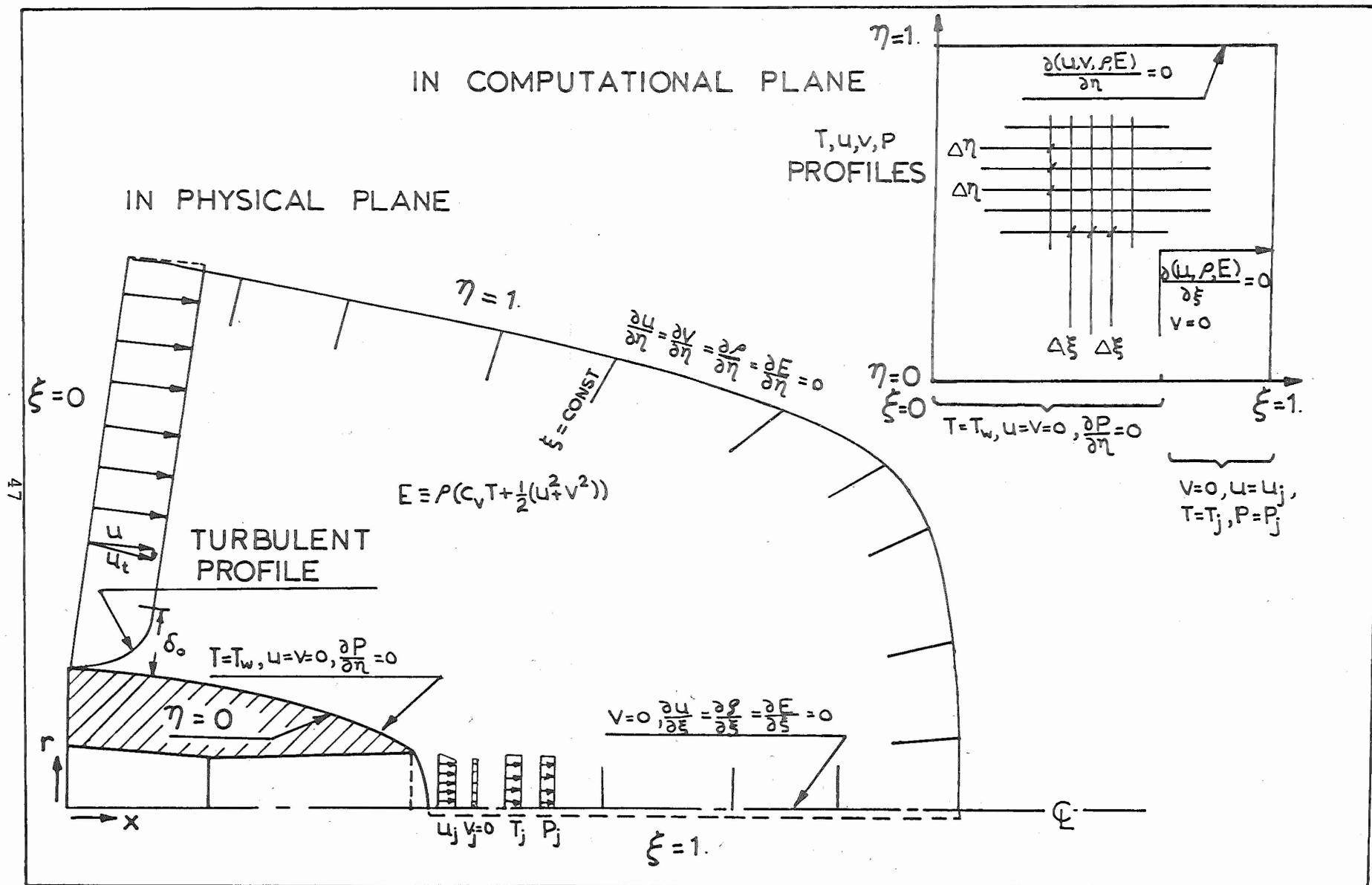


Figure 14. Boundary Conditions in the Physical and Computational Domain.

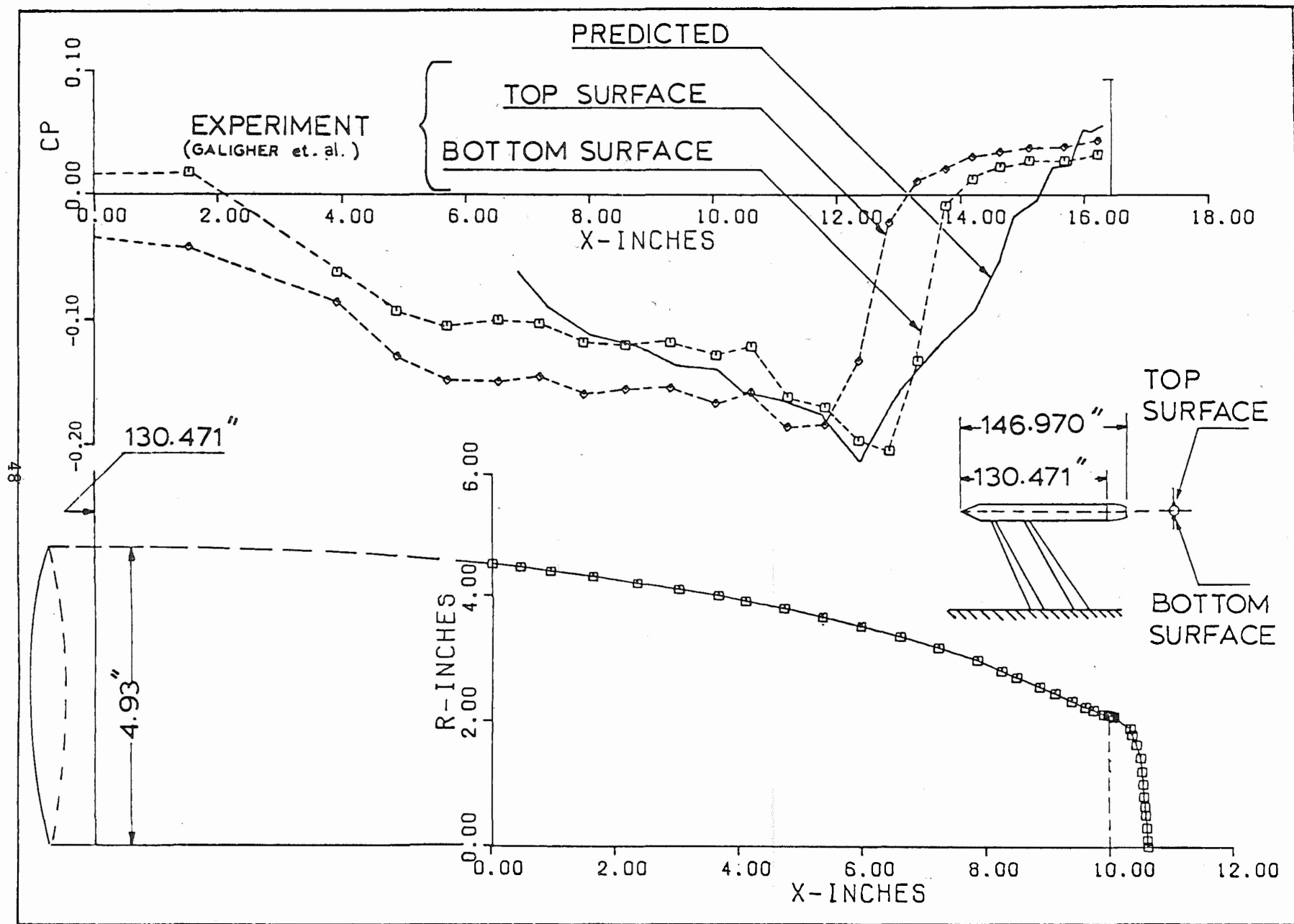


Figure 15. Comparison with Experiment.

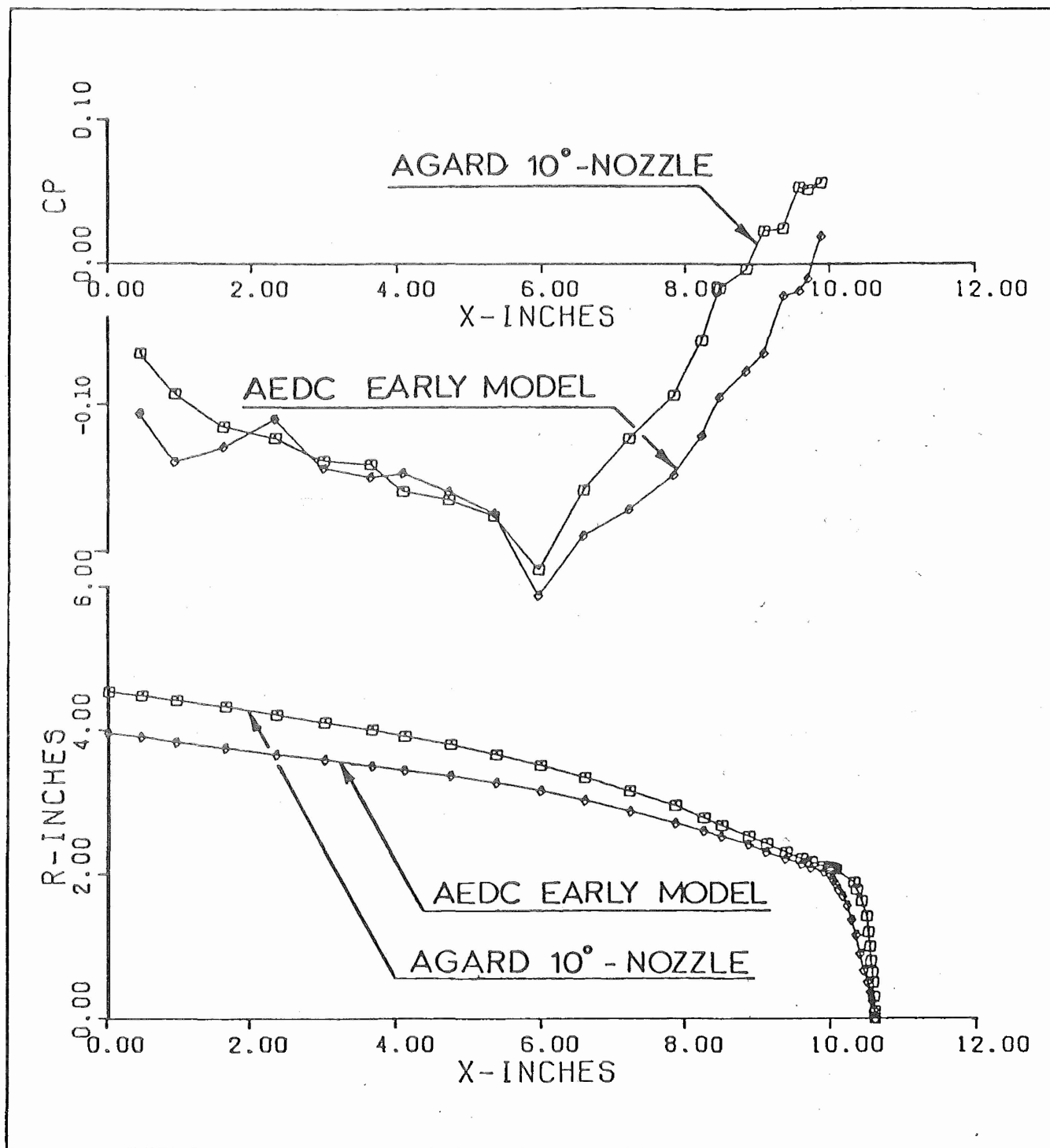


Figure 16. Influence of Boattail Geometry on Pressure Coefficient Distribution.

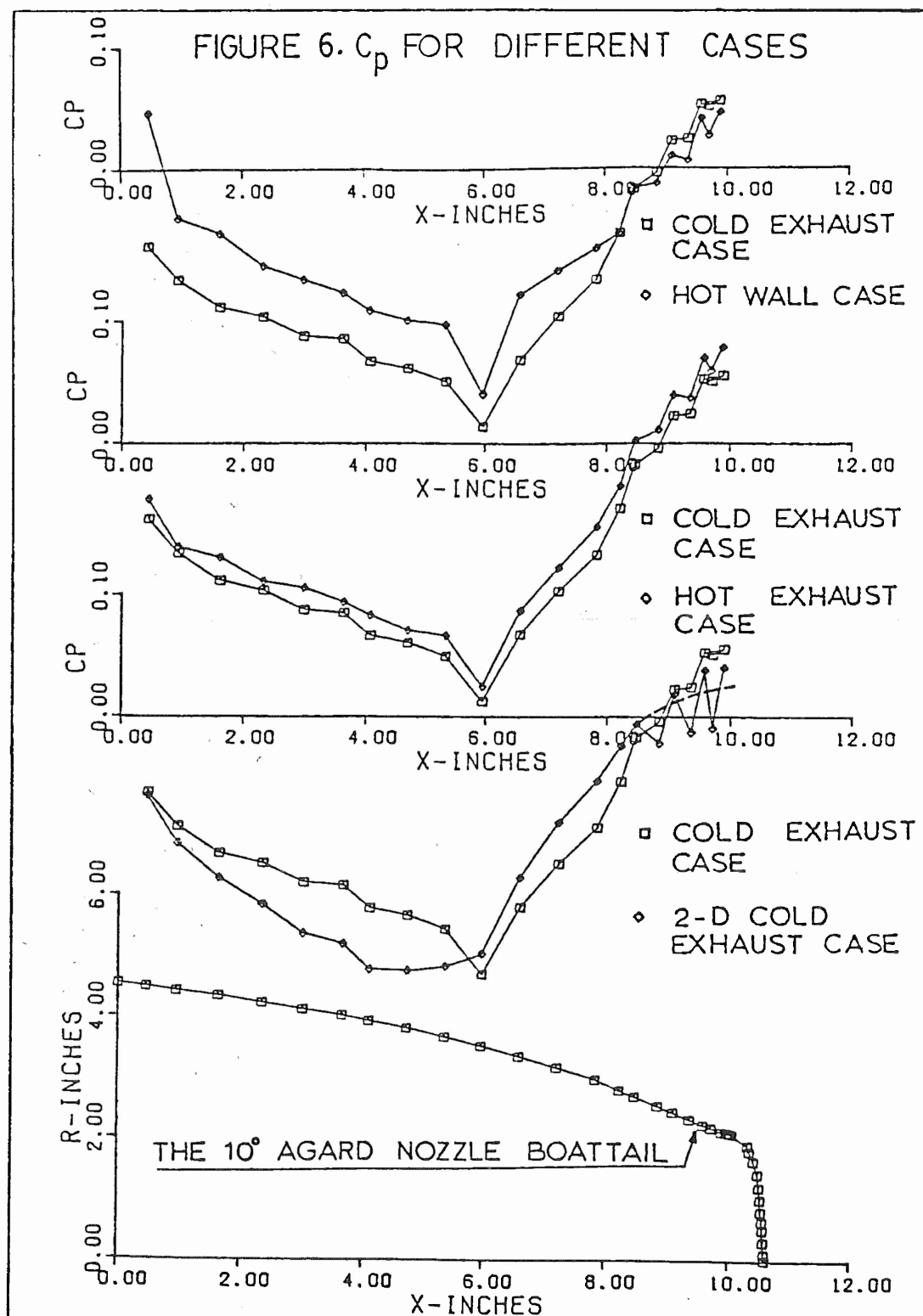


Figure 17.  $C_p$  For Different Cases.

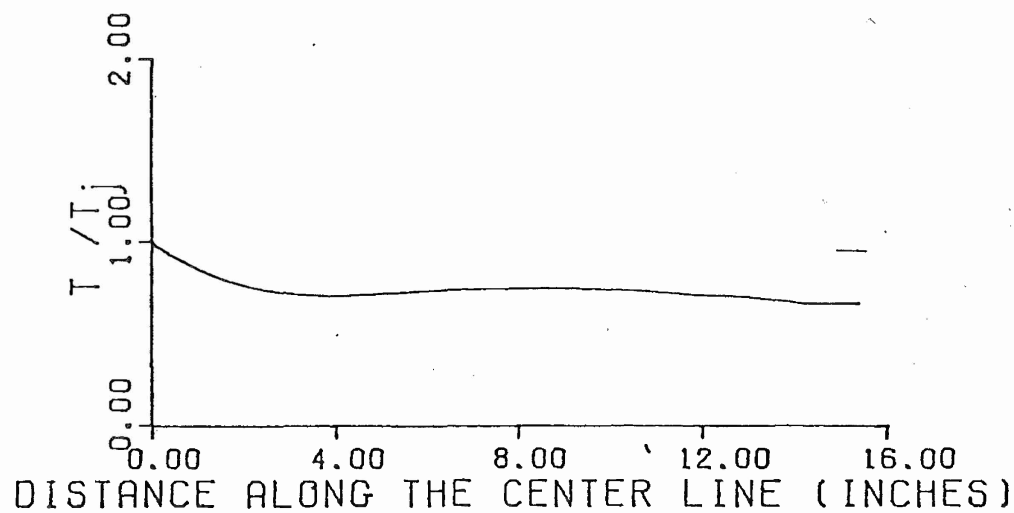
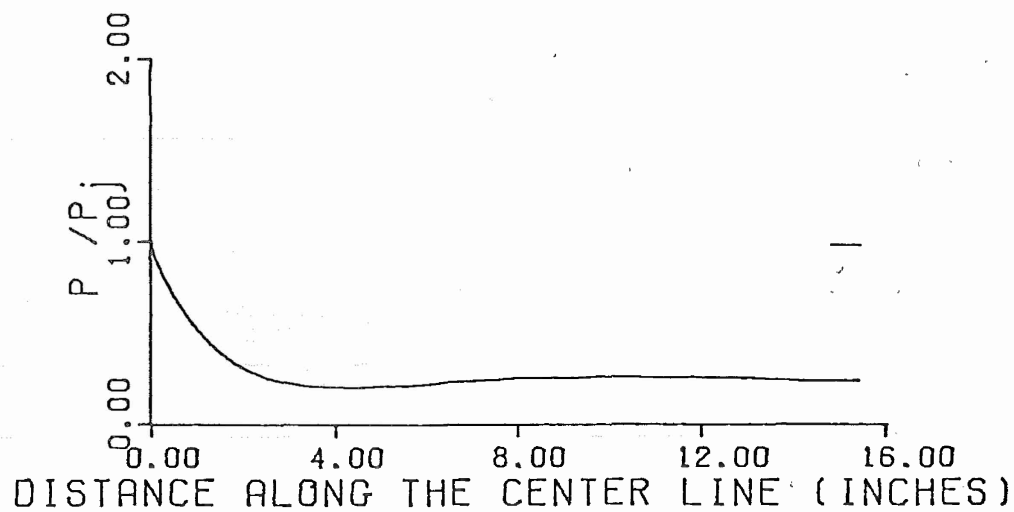
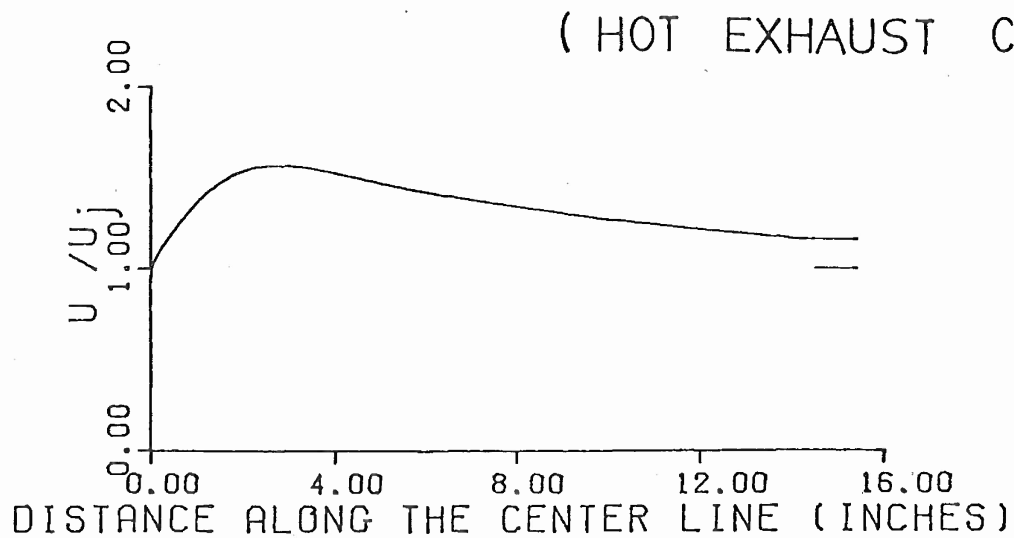


Figure 18. Axial Variation in  $u$ ,  $p$  &  $T$ .

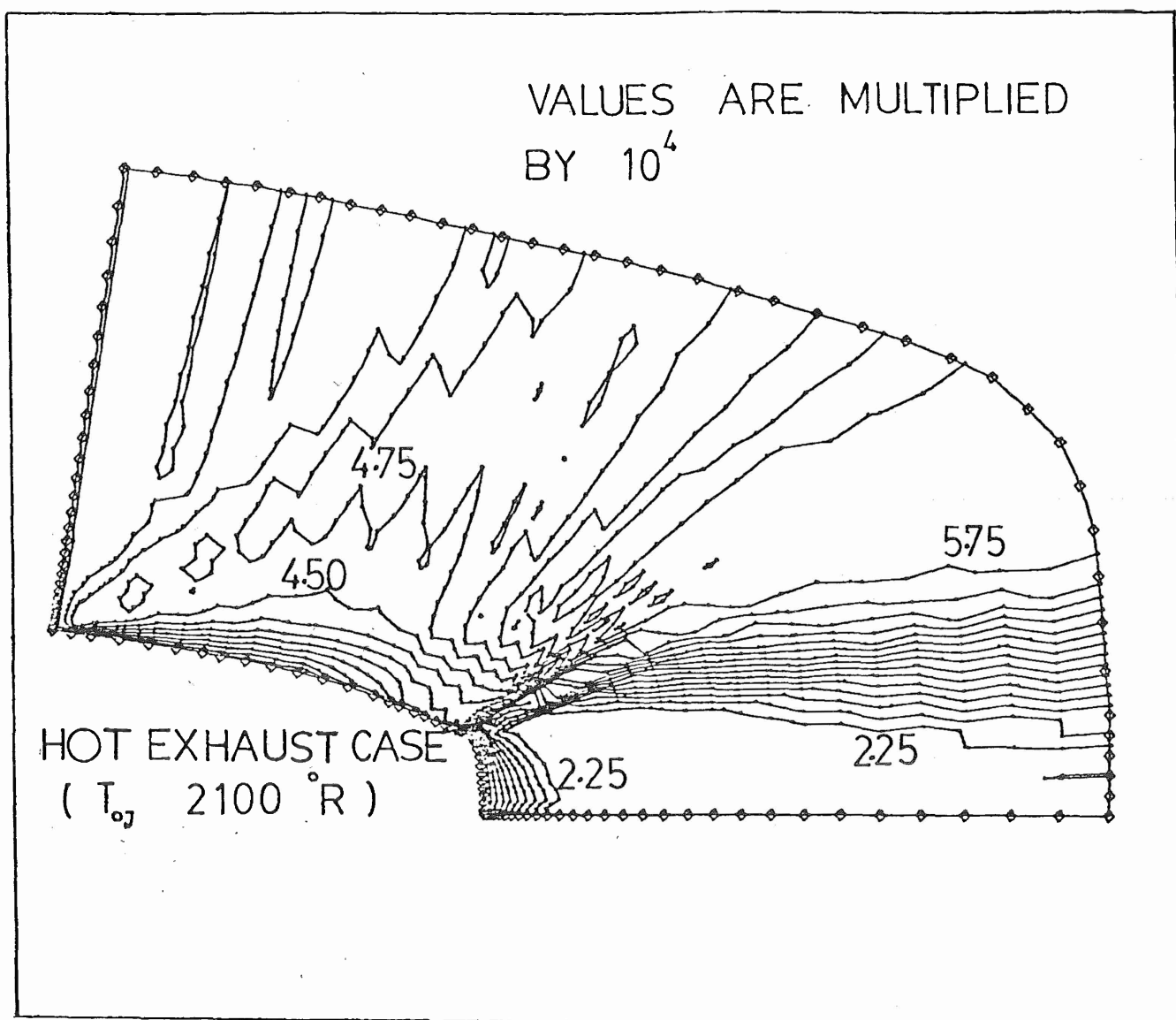


Figure 19. Density Contours.

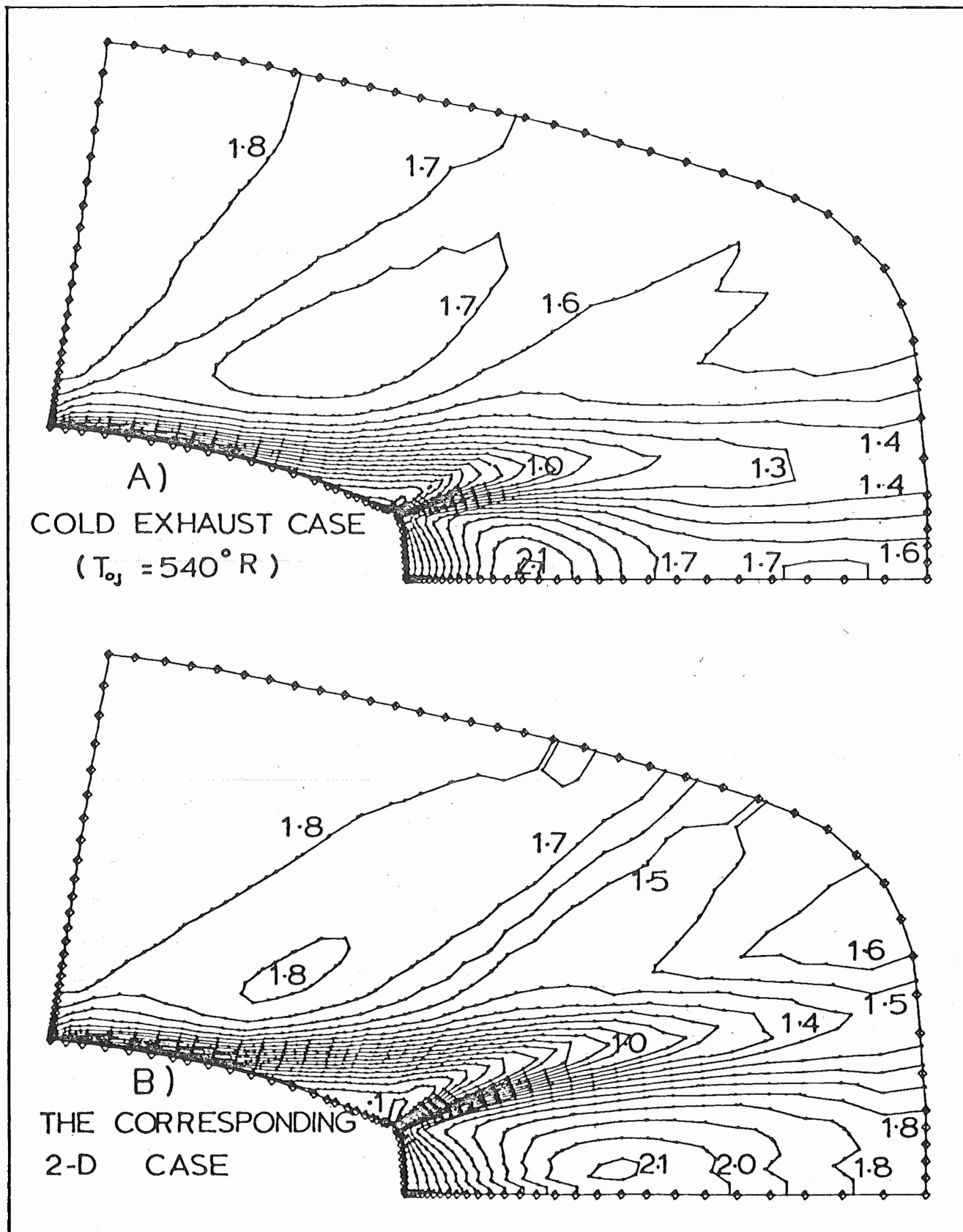


Figure 20. Mach-Line Contours.

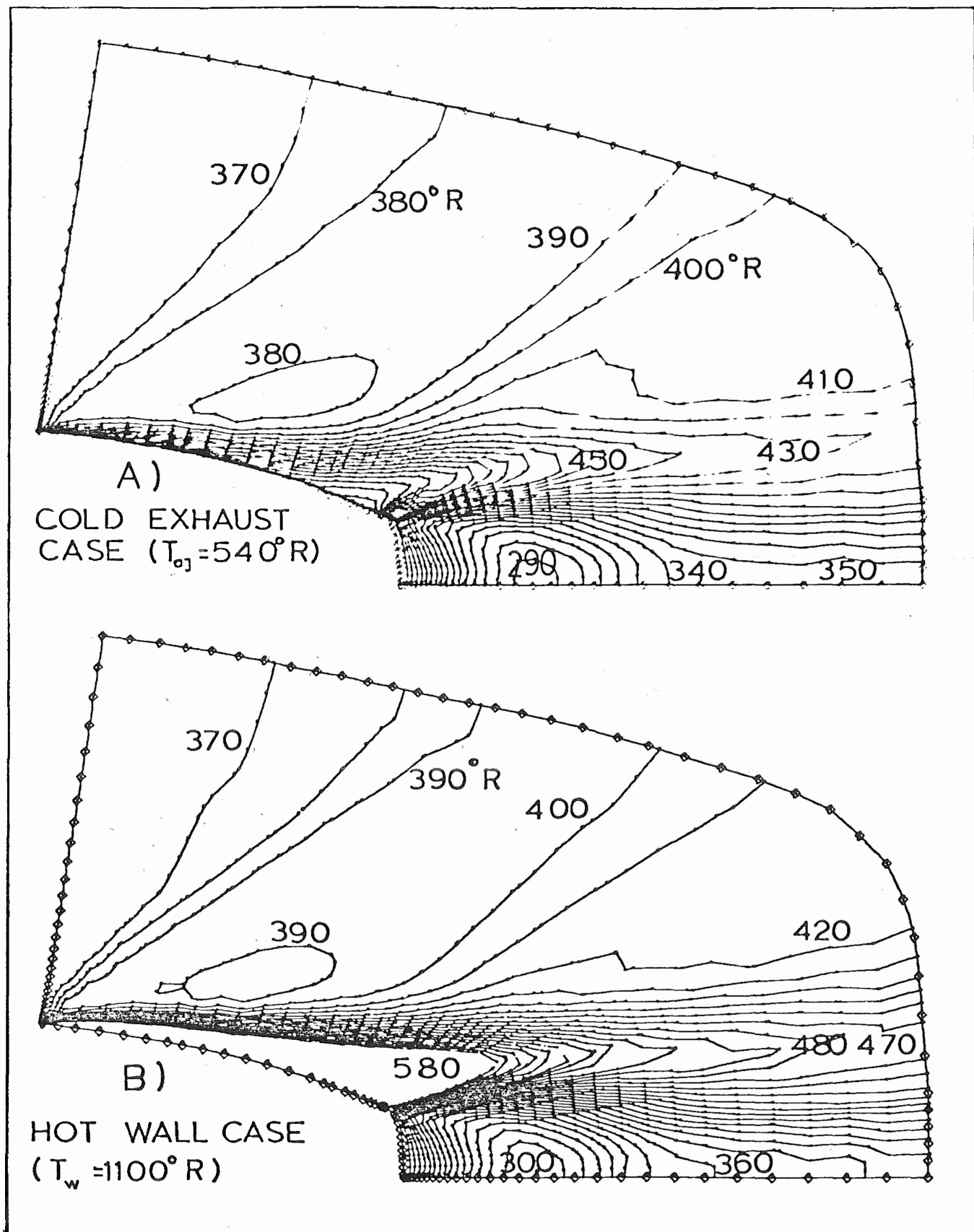


Figure 21. Static Temperature Contours.



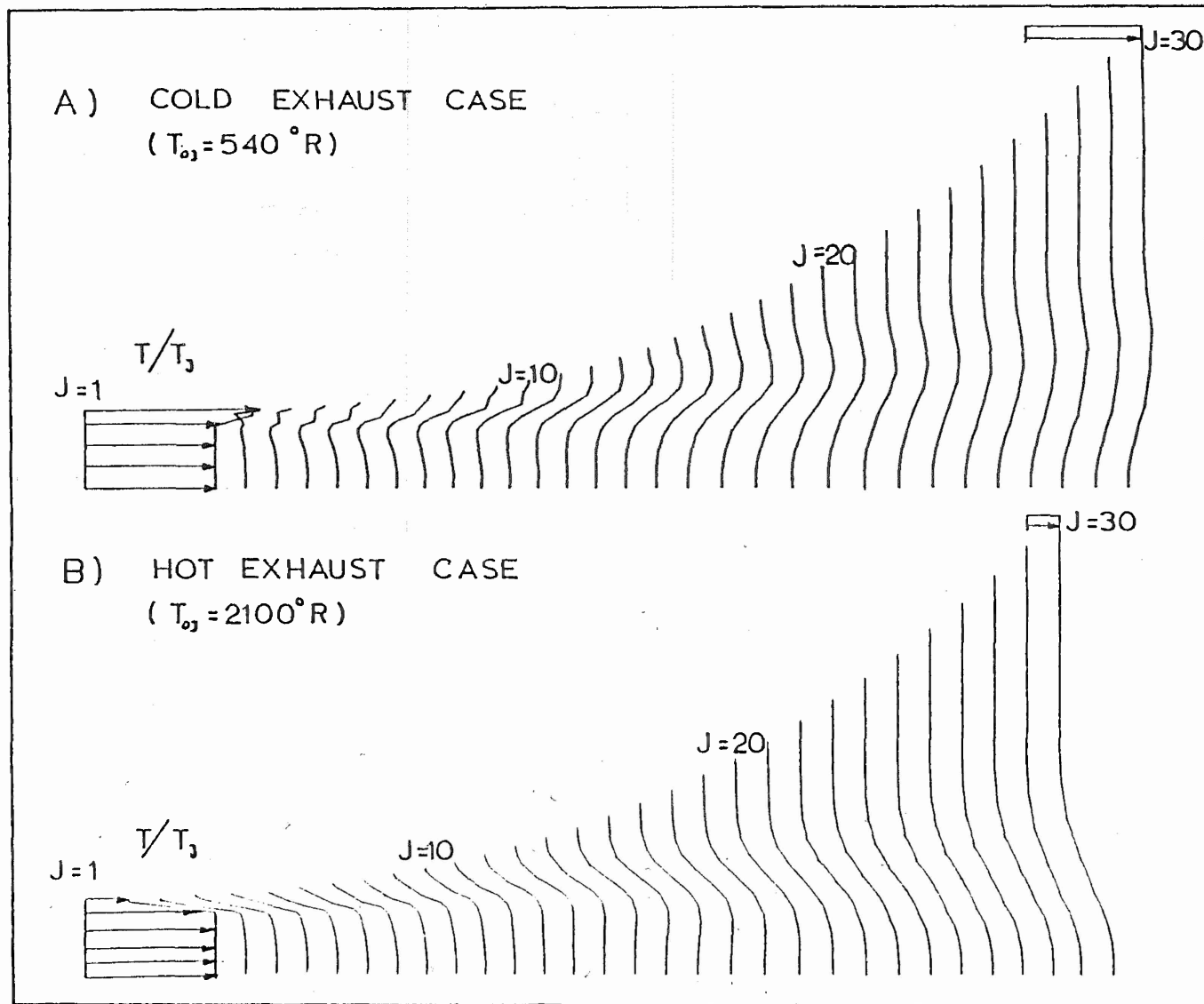


Figure 22. Static Temperature Profiles in the Mixing Region.

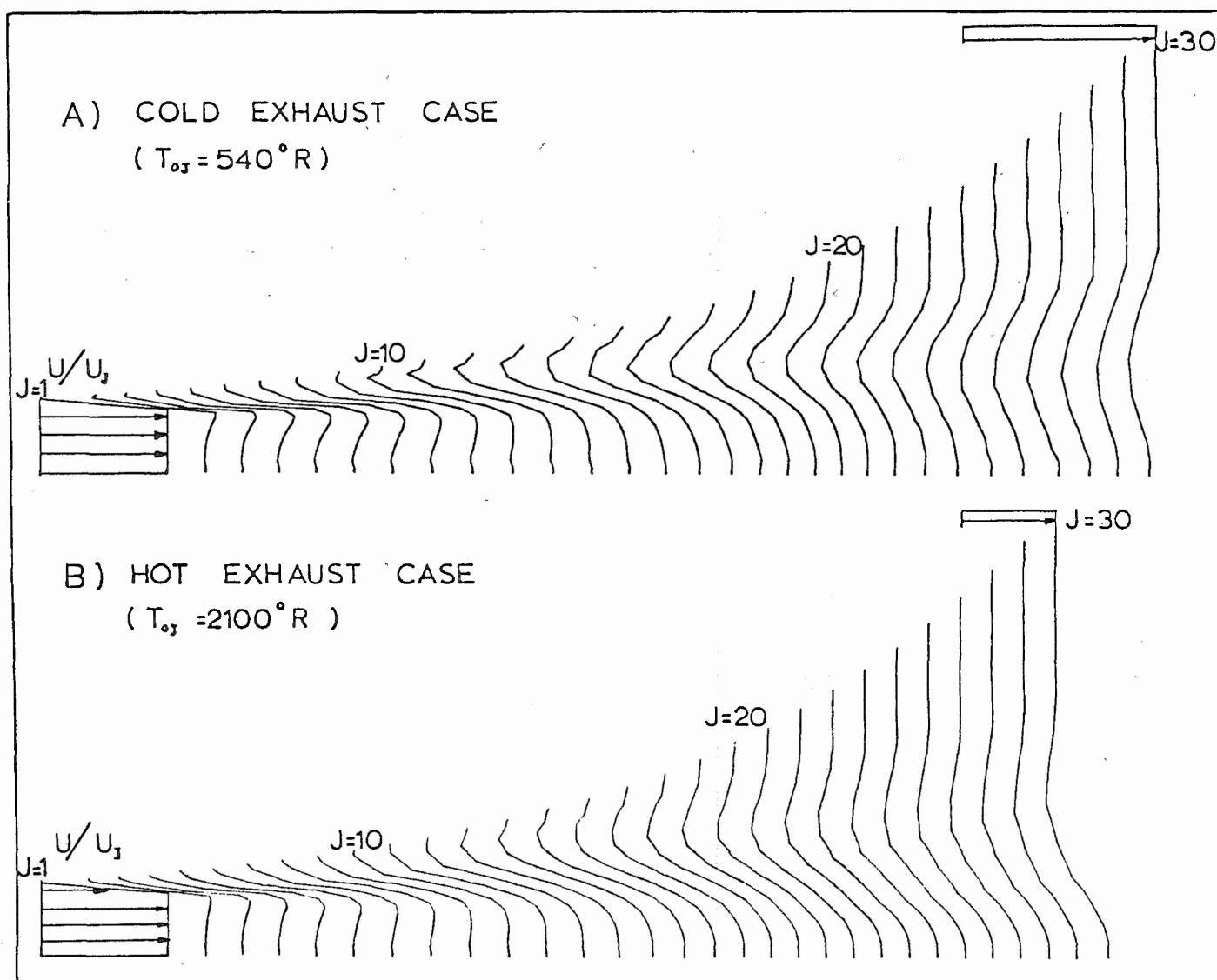


Figure 23. Axial-Velocity Profiles in the Mixing Region.

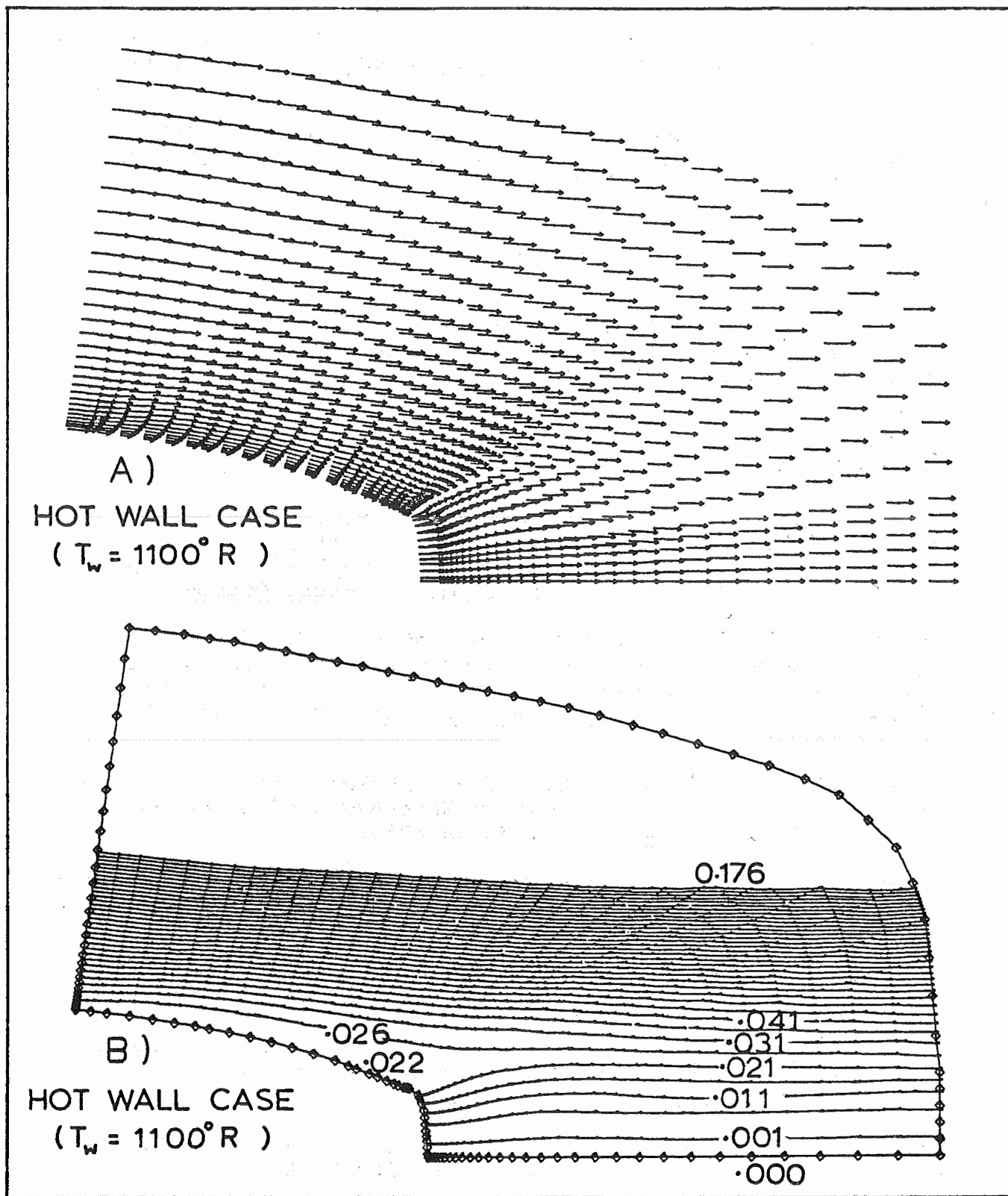


Figure 24. The Flow Field and Stream Function.

## REFERENCES

1. Holst, T.L., "Numerical Solution of Axisymmetric Boattail Fields with Plume Simulators," AIAA Paper 74-224, January 1977.
2. Cosner, R.R. and Bower, W.W., "A Patched Solution of the Transonic Flow Field About an Axisymmetric Boattail," AIAA Paper 77-227, January 1977.
3. Yaros, S.F., "Prediction of Pressure Distributions on Axisymmetric Bodies in Transonic Flow," AIAA Paper 77-226, January 1977.
4. Knight, D.D., "Numerical Simulation of High Speed Inlets Using the Navier-Stokes Equations," AIAA J., Vol. 15, No.11, November 1977, pp. 1583-1589.
5. Segalman, I. and Semerjian, H., "Turbine Engine Infrared Signature Program - Final Report," AFAPL-TR-76-38, Air Force Aero Propulsion Laboratory, Dayton, Ohio, June 1976.
6. Galigher, L.L., Yaros, S.F., and Bauer, R.C., "Evaluation of Boattail Geometry and Exhaust Plume Temperature Effects on Nozzle Afterbody Drag at Transonic Mach Numbers," AEDC-TR-76-102, Arnold Engineering Development Center, October 1976.
7. Thompson, J.F., Thames, F.C., and Mastin, W.C., "Automatic Numerical Generation of Body-Fitted Curvilinear Coordinate System for Field Containing any Number of Arbitrary Two-Dimensional Bodies," J. of Computational Physics, 15, 1974, pp. 299-319.
8. Rubesin, M.W. and Rose, W.C., "The Turbulent Mean-Flow Reynolds Stress and Heat-Flux Equations in Mass-Averaged Dependent Variables," NASA TM X-62,248, March 1973.
9. McRae, D.S., "The Conically Symmetric Navier-Stokes Equations: Numerical Solution for Hypersonic Cone Flow at High Angle of Attack," AFFDL-TR-76-139, March 1977.
10. Viviani, H., "Conservation Forms of Gas Dynamics Equations," La Recherche Aerospatiale, No. 1, Jan.-Feb., 1974, pp. 65-66.
11. "Free Turbulent Shear Flows," Volume I - Conference Proceedings, Proceedings of a conference held at Langley Research Center, July 20-21, 1972, NASA SP-321, 1973.
12. "Symposium on Turbulent Shear Flows," April 18-20, 1977, Pennsylvania State University, University Park, Pennsylvania.

# REFERENCES (Concluded)

13. Cebeci, T., Smith, A.M.O. and Mosinskis, G., "Calculations of Compressible Adiabatic Turbulent Boundary Layers," AIAA J., Vol. 8, No. 11, 1970.
14. Peters, C.E. and Phares, W.J., "Analytical Model of Supersonic, Turbulent Near-Wake Flows," AEDC-TR-76-127, Arnold Engineering Development Center, September 1976.
15. Issa, R.I. and Lockwood, F.C., "On the Prediction of Two-Dimensional Supersonic Viscous Interactions Near Walls," AIAA J., Vol. 15, No. 2, Feb. 1977, pp. 182-188.
16. MacCormack, R.W., "Numerical Solution of the Interaction of Shock Wave with a Laminar Boundary Layer," Lecture Notes in Physics, Vol. 8, Springer-Verlag, 1971, pp. 151-163.
17. MacCormack, R.W. and Baldwin, B.S., "A Numerical Method for Solving the Navier-Stokes Equations with Application to Shock-Boundary Layer Interactions," AIAA Paper 75-1, Jan. 1975.
18. MacCormack, R.W. and Paullay, A.G., "Computational Efficiency Achieved by Time Splitting of Finite Difference Operators," AIAA Paper 72-154, 1972.
19. Shang, J.S., Private Communications.
20. Mikhail, A.G., Hankey, W.L. and Shang, J.S., "Computation of a Supersonic Flow Past an Axisymmetric Nozzle Boattail with Jet Exhaust," AIAA Paper 78-993, Presented in Las Vegas during the AIAA/ASE 14th Joint Propulsion Conference, July 25-27, 1978.
21. Beam, R.M. and Warming, R.F., "An Implicit Factored Scheme for the Compressible Navier-Stokes Equations," AIAA J., Vol. 16, No. 4, April 1978, pp. 393-402.
22. Shang, J.S., "A Hybrid Implicit-Explicit Numerical Technique for Solving the Navier-Stokes Equations," AIAA Paper 77-646, June 1977.
23. Griffin, M.D. and Anderson, J.D., "On the Application of Boundary Conditions to Time Dependent Computations for Quasi One-Dimensional Fluid Flows," Computers and Fluids, Vol. 5, 1977, pp. 127-137.
24. Auld, D.J. and Bird, G.A., "Monte Carlo Simulation of Regular and Mach Reflection," AIAA J., Vol. 15, No. 5, June 1977, pp. 638-641.